

Contents

2	1 Arcadia-MD1	2
3	1.1 The sensor	2
4	1.1.1 Two different FE flavor	3
5	1.2 Readout logic and data structure	3
6	1.2.1 Matrix division and data-packets	3
7	2 Characterization	7
8	2.1 TJ-Monopix1 characterization	7
9	2.1.1 Threshold and noise: figure of merit for pixel detectors	7
10	2.1.2 Linearity of the ToT	11
11	2.1.3 Calibration of the ToT	12
12	2.1.4 Changing the bias	17
13	2.1.5 Measurements with radioactive sources	18
14	2.1.6 Dead time measurements	23
15	2.2 ARCADIA-MD1 characterization	25
16	3 Test beam measurements	29
17	3.1 Apparatus description	30
18	3.1.1 Accelerator	30
19	3.1.2 Mechanical carriers	30
20	3.2 Measurements	31
21	Bibliography	36
22	Characterization of monolithic CMOS pixel sensors for charged particle detectors and	
23	for high intensity dosimetry	

²⁴ **Chapter 1**

²⁵ **Arcadia-MD1**

²⁶ [16] [17]

²⁷ Breve introduzione analoga a Monopix1 in cui descrivo brevemente la "timeline" da
²⁸ SEED Matisse a Md1 e Md2

²⁹ Tutti i minid, siano essi v1 o v2, sono Alpide like. Prima SEED si occupa di stu-
³⁰ diare le prestazioni: concept study with small-scale test structure (SEED), dopo arcadia:
³¹ technology demonstration with large area sensors Small scale demo SEED(sensor with em-
³² bedded electronic developement) Quanto spazio dato all'elettronica sopra il pwell e quanto
³³ al diodo. ..

³⁴ **1.1 The sensor**

³⁵ ARCADIA-MD1 is an LFoundry chip which implements the technology 110 nm CMOS
³⁶ node with six metal layer **??**. The standard p-type substrate was replaced with an n-type
³⁷ floating zone material, that is a tecnique to produce purified silicon crystal. (pag 299
³⁸ K.W.).

³⁹ Tra i wafer fabbricati finora ci sono 3 valori di spessore attivo nominale (lo spessore
⁴⁰ effettivo può variare di qualche micron ripetto a quello nominale): 48um, 100um e 200um.
⁴¹ In allegato un'immagine con le cross section.

⁴² Wafer thinning and backside lithography were necessary to introduce a junction at the
⁴³ bottom surface, used to bias the substrate to full depletion while maintaining a low voltage
⁴⁴ at the front side.

⁴⁵ C'è un deep pwell per - priority chain separare l'elettronica dal sensore; per controllare il
⁴⁶ punchthought è stato aggiunto un n doped epitaxial layer having a resistivity lower than
⁴⁷ the substrate. It is part of the cathegory of DMAPS Small electrode to enhance the signal

Parameter	Value
Matrix size	$\times \text{ cm}^2$
Pixel size	$25 \times 25 \mu\text{m}^2$
Depth	? μm
Electrode size	$9 \times 9 \mu\text{m}^2$
Power consumption	$\sim \text{ mW/cm}^2$

Table 1.1

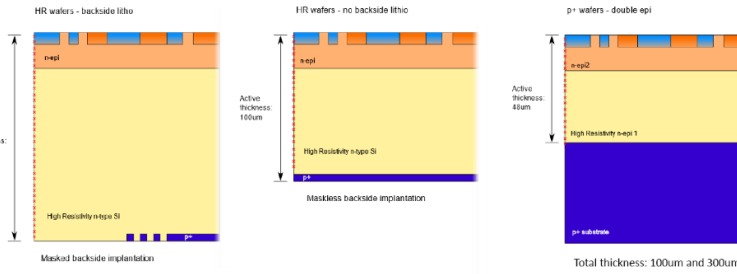


Figure 1.1

48 to noise ratio. It is operated in full depletion with fast charge collection by drift.

49 1.1.1 Two different FE flavor

50 Le differenze tra Alpide e bulk driven sono un po' più complesse di quanto hai scritto.
 51 Si tratta proprio di due architetture diverse. Il primo amplifica il segnale attraverso il
 52 trasferimento di carica tra due capacità. Nel bulk driven invece il guadagno è dato dal
 53 rapporto tra due transconduttanze. Inoltre ci sono altre differenze, il bulk driven è più
 54 sensibile alle cadute di tensione sul ground (che ahimè è esattamente ciò che accade nei
 55 dimostratori che abbiamo ora, a causa dell'anomalo consumo di corrente dal digitale,
 56 altro baco che abbiamo corretto nella terza sottomissione). Anche i livelli di tensione nei
 57 nodi interni dei due front-end differiscono e il meccanismo di clipping che funzionava per
 58 l'Alpide non è applicabile al bulk driven. Di conseguenza abbiamo un bias in più (ICLIP)
 59 nel secondo flavour per controllare il clipping. Nell'Alpide il clipping c'è, ma l'architettura
 60 usata permette di non aver bisogno di un bias esterno, anche se in una versione di Alpide
 61 di ALICE hanno scelto di controllare comunque la corrente di clip esternamente, per una
 62 maggiore flessibilità. Infine alcuni bias che hanno lo stesso nome nei due flavour, perché
 63 svolgono la stessa funzione, differiscono nel valore di configurazione didefault.

64 1.2 Readout logic and data structure

65 In order to achieve the lowest possible power consumption, the matrix is clockless, no
 66 free-running clock, and to save as much area as possible, it will not buffer any hits, and
 67 its readout will thus be triggerless.

68 The Periphery has both an analog part, segmented per Section, and a digital part,
 69 which is instead shared. The analog part hosts the bias cells for the AFE dei pixel, mentre
 70 la parte digitale che è unica per tutti riprocesso le hit che vengono dalle sezioni e 8b10b
 71 encode le parole per data transmission.

72 1.2.1 Matrix division and data-packets

73 The matrix is divided into an internal physical and logical hierarchy: The 512 columns are
 74 divided in 16 section: 512×32 pixels, each section has different voltage-bias + serializzatori.
 75 Each section is devided 512×2 column, and in 32×2 core: in modo che in ogni doppia
 76 colonna ci siano 1Pacchetto dei dati 6 cores. ricordati dei serializzatori: sono 16 ma
 77 possono essere ridotti ad uno in modalità spazio Ed infine regioni da 4×2 . The readout
 78 design must be capable of addressing the following matters Enough bus bandwidth for a

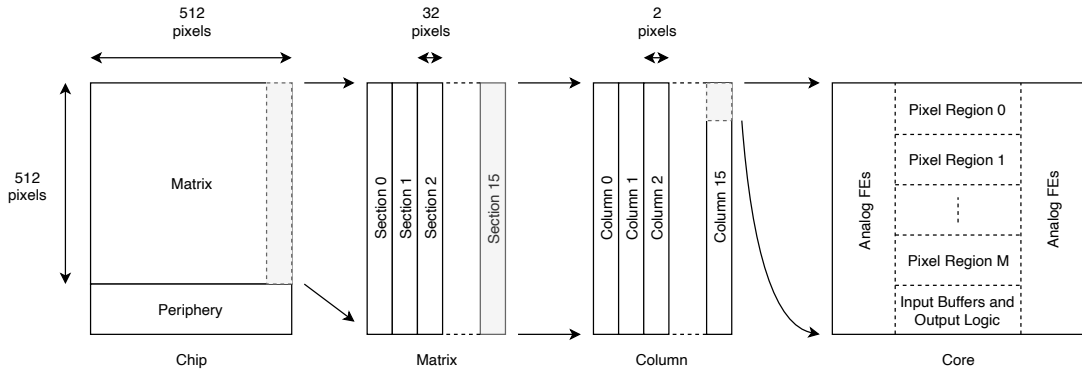


Figure 1.2

79 hit rate of 100 MHz/cm². Design decisions: Try and send as much data as possible to the
80 periphery (bandwidth) Lowest amount of logic possible (more routability)

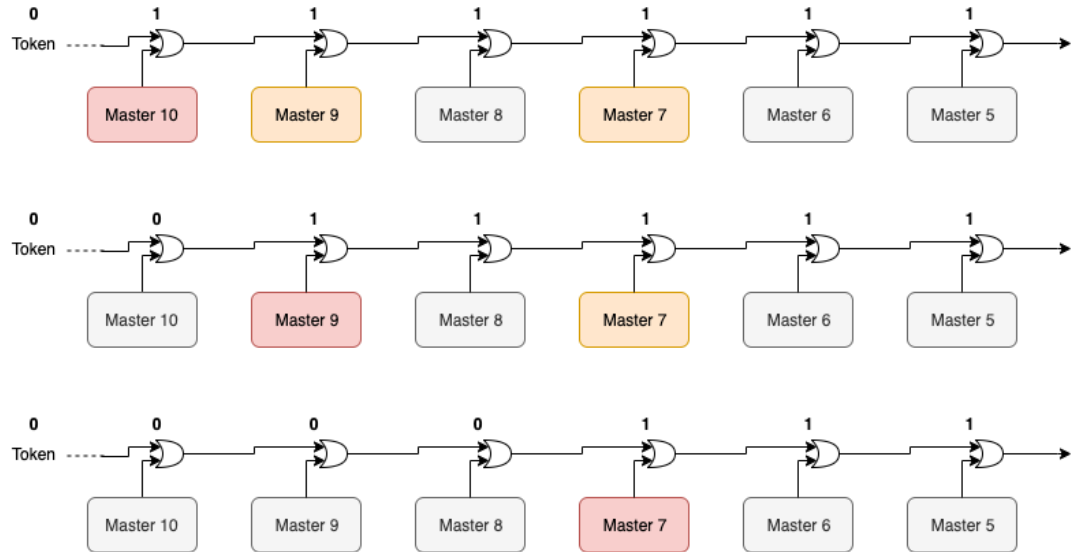


Figure 1.3

81 Questa divisione si rispecchia in come sono fatti i dati: scrivi da quanti bit un dato è
82 fatto e le varie coordinate che ci si trovano dentro; devi dire che c'è un pixel hot e spieghi
83 dopo a cosa serve, e devi accennare al timestamp

84 "A core is simply the smallest stepped and repeated instance of digital circuitry. A
85 relatively large core allows one to take full advantage of digital synthesis tools to imple-
86 ment complex functionality in the pixel matrix, sharing resources among many pixels as
87 needed.". pagina 28 della review.

88

89 TABELLA: con la gerarchia del chip Matrix (512x512 pixels) Section (512x32 pixels)
90 Column (512x2) Core (32x2) Region (4x2)

91 Nel chip trovi diverse padframe: cosa c'è nelle padframe e End of section.

92 "DC-balance avoids low frequencies by guaranteeing at least one transition every n
93 bits; for example 8b10b encoding n =5"

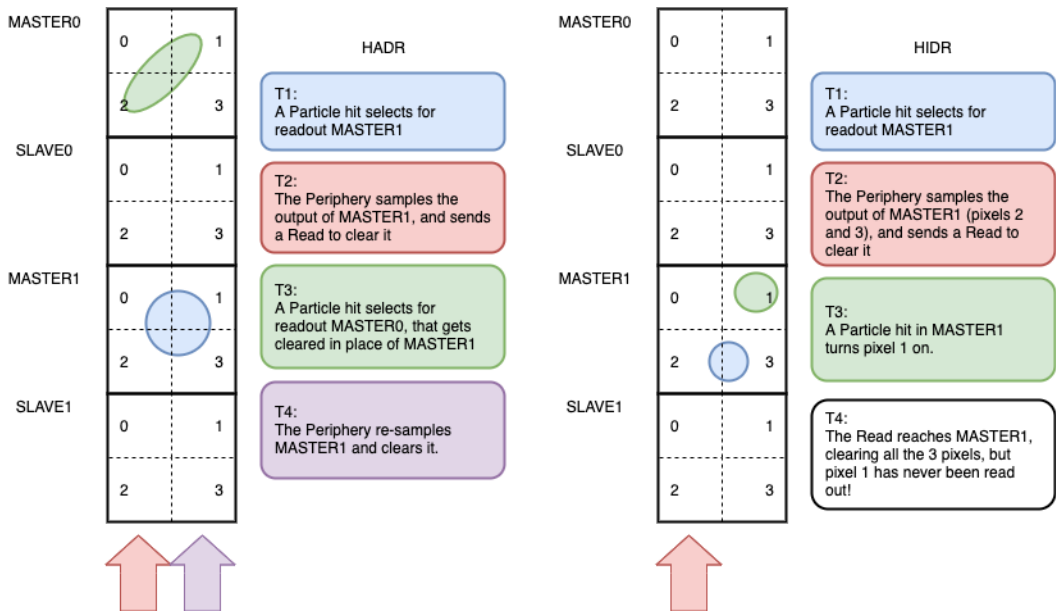


Figure 1.4

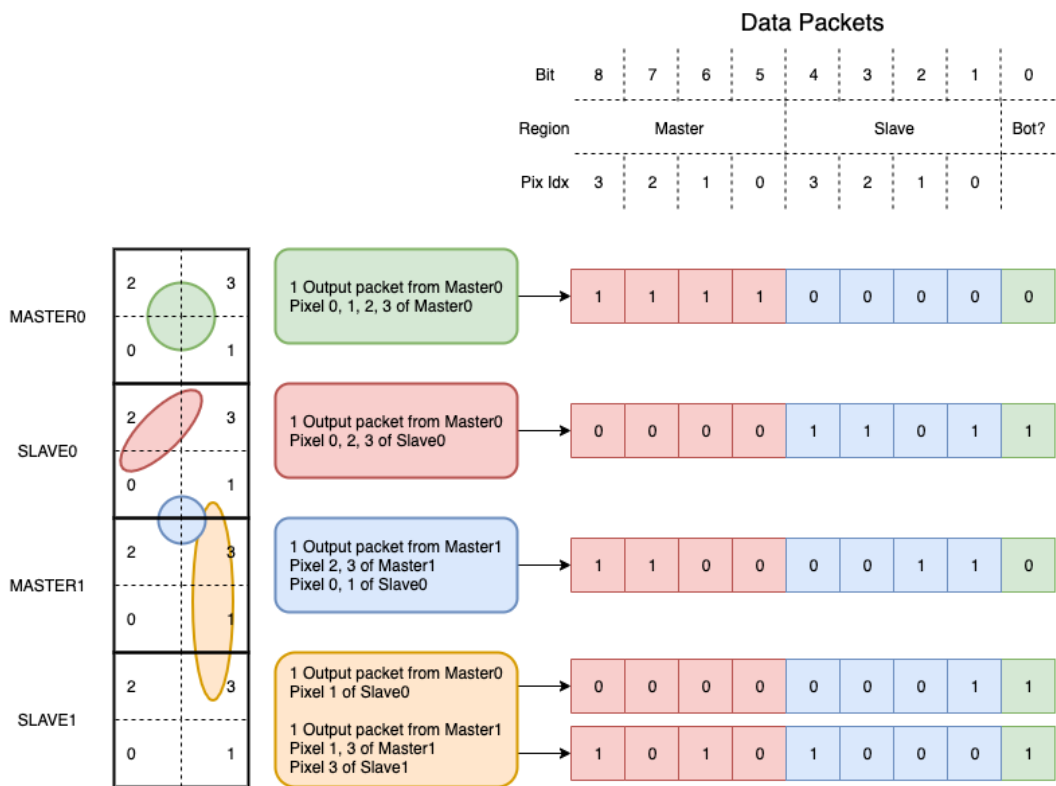


Figure 1.5

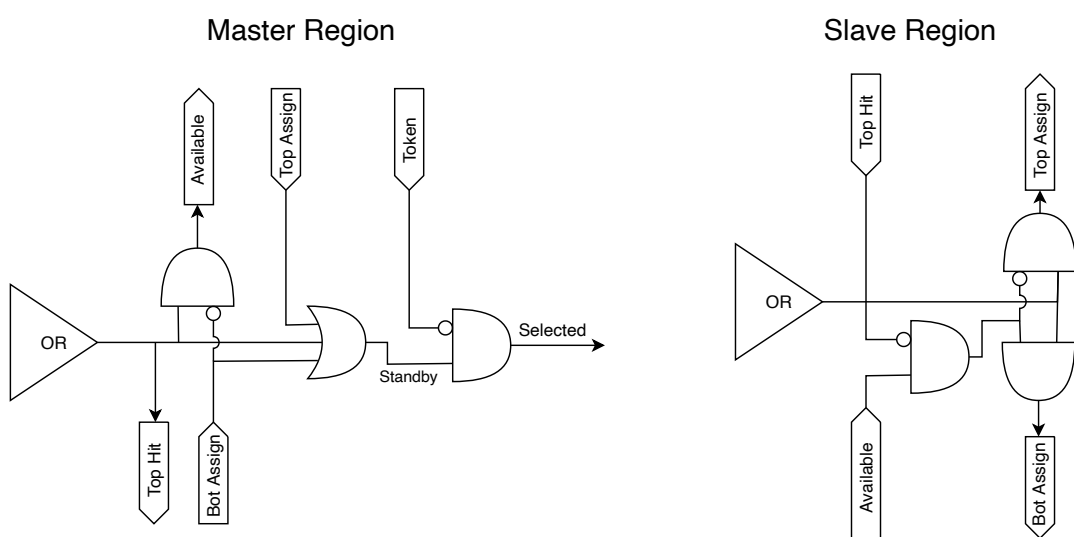


Figure 1.6

⁹⁴ **Chapter 2**

⁹⁵ **Characterization**

⁹⁶ Rifai il conto della lunghezza di attenuazione. Ho trovato (presentazione Luciano Mus) 29
⁹⁷ um per ka e 37 um per kb.

⁹⁸ **2.1 TJ-Monopix1 characterization**

⁹⁹ **2.1.1 Threshold and noise: figure of merit for pixel detectors**

¹⁰⁰ A characterization of threshold and noise is typically necessary since these values have an
¹⁰¹ impact on the operating conditions and on the performance of the chips, so much that
¹⁰² the signal to threshold ratio may be considered as the figure of merit for pixel detectors
¹⁰³ rather than the signal to noise ratio. The mean minimum stable threshold evolved through
¹⁰⁴ different generation of chips: in the 1st generation it was around 2500 e^- while in the 3rd
¹⁰⁵ (corresponding to nowadays chips) is less than 500 e^- . This allows in thinner sensors with
¹⁰⁶ smaller signals: from $16\,000 \text{ e}^-$ produced in $200 \mu\text{m}$, the signal expected moved down to
¹⁰⁷ 2000 e^- produced in $25 \mu\text{m}$. In agreement with this, the threshold of TJ-Monopix1 is
¹⁰⁸ around 500 e^- .

¹⁰⁹ Obviously the threshold has to be located between the noise peak around the baseline
¹¹⁰ and the signal distribution, in particular it has to be low enough to maintain a high signal
¹¹¹ efficiency, but also high enough to cut the noise: for a low threshold many pixels can fire
¹¹² at the same time and a positive feedback can set off a chain reaction eventually, causing
¹¹³ all the other pixels to fire. Thus, the noise sets a lower bound to the threshold: if an
¹¹⁴ occupancy $\leq 10^{-4}$ is required, for example, a probability of firing lower than that value
¹¹⁵ is needed and this, assuming a gaussian noise, requires that the threshold is set at least
¹¹⁶ 3.7σ , with σ the RMS of the noise. In this case, if the noise is 100 e^- (reasonable), the
¹¹⁷ threshold must be higher than $3.7 \times 100 \text{ e}^-$. Typically this argument sets only a minimal
¹¹⁸ bound to the threshold since the variation with time and from pixel to pixel have to be
¹¹⁹ taken into account: the temperature, the annealing (for example, the radiation damages in
¹²⁰ the oxide layer causes shift of MOSFET threshold voltage) and the process parameters
¹²¹ variation across the wafer (as for example process mismatch between transistors).

¹²² On the other hand, concerning the noise, given that the first stage of amplification is
¹²³ the most crucial, since in the following stages the signal amplitude is high compared to
¹²⁴ additional noise, it is valued at the preamplifier input node. Then, the noise is parame-
¹²⁵ terized as Equivalent Noise Charge (ENC), which is defined as the ratio between the noise
¹²⁶ N at the output expressed in Volt and the out voltage signal S produced by 1 e^- entering

127 in the preamplifier:

$$ENC = \frac{N_{out}[V]}{S_{out}[V/e-]} = \frac{V_{noise}^{RMS}}{G} \quad (2.1)$$

128 with G expressed in V/e-; as the gain increases, the noise reduces .

129 Considering the threshold dispersion a requirement for the ENC is:

$$ENC < \sqrt{(T/3.7)^2 - T_{RMS}^2(x) - T_{RMS}^2(t)} \quad (2.2)$$

130 where the T is the threshold set, T_{RMS} is the threshold variation during time (t) and
131 across the matrix (x); a typical reasonable value often chosen is 5 ENC.

132 Because of the changing of the 'real' threshold, the possibility of changing and adapting
133 the setting parameters of the FE, both in time and in space is desiderable: these parameters
134 are usually set by Digital to Analog Converter (DAC) with a number of bit in a typical
135 range of 3-7. Unfortunately DAC elements require a lot of space that may be not enough
136 on the pixel area; therefore, the FE parameters are typically global, which means that they
137 are assigned for the whole chip, or they can be assigned for regions the matrix is divided
138 into. The former case corresponds to TJ-Monopix1's design in which 7 bits are used for
139 a total 127-DAC possible values, while the latter corresponds to the ARCADIA-MD1's
140 one, **where quanti bit??**. An other possibility, for example implemented in TJ-Monopix2,
141 is allocate the space on each pixel for a subset of bits, then combinig the global threshold
142 with a fine tuning. If so, the threshold dispersion after tuning is expected to decrease
143 depening on the number of bits available for tuning:

$$\sigma_{THR,tuned} = \frac{\sigma_{THR}}{2^{nbit}} \quad (2.3)$$

144 where σ_{thr} is the RMS of the threshold spread before tuning.

145 To measure the threshold and noise of pixels a possible way is to make a scan with
146 different known injected charge: the threshold corresponds to the value where the efficiency
147 of the signal exceeds the 50%, and the ENC is determined from the slope at this point.
148 Assuming a gaussian noise, e.g. a noise whose transfer function turns a voltage δ pulse in a
149 gaussian distribution, the efficiency of detecting the signal and the noise can be described
150 with the function below:

$$f(x, \mu, \sigma) = \frac{1}{2} \left(1 + erf \left(\frac{x - \mu}{\sigma\sqrt{2}} \right) \right) \quad (2.4)$$

151 where erf is the error function. Referring to 2.4 the threshold and the ENC corresponds
152 to the μ and σ .

153 I used the injection circuit available on the chip to inject 100 pulses for each input
154 charge for a fixed threshold. The injection happens on a capacity at the input of the FE
155 circuit, whose nominal value is 230 aF and from which the conversion factor from DAC
156 units to electrons can be obtained: for the PMOS flavor, for example, since the DAC are
157 biased at 1.8 V, the Least significant Bit (LSB) corresponds to a voltage of 14.7 mV from
158 which the charge for LSB $1.43 \text{ e-}/\text{mV}$ and the conversion factor therefore is $20.3 \text{ e-}/\text{DAC}$.
159 While this value is equivalent for all the PMOS flavor, the HV flavor is expected to have a
160 different conversion factor, $\sim 33 \text{ e-}/\text{DAC}$, beacuse of the different input capacity. Besides
161 the charge, also the duration and the period of the injection pulse can be set; it is important
162 to make the duration short enough to have the falling edge during the dead time of the
163 pixel (in particular during the FREEZE signal) in order to avoid the undershoot, coming

	PMOS A	PMOS B	PMOS C	HV
Threshold [e ⁻]	401.70±0.15	400.78±0.24	539.66±0.58	403.87±0.19
Threshold dispersion [e ⁻]	32.90±0.11	32.97±0.17	55.54±0.42	44.67±0.15
Noise [e ⁻]	13.006±0.064	12.258±0.068	13.88±0.11	11.68±0.10
Noise dispersion [e ⁻]	1.608±0.044	1.504±0.046	1.906±0.072	1.580±0.068

Table 2.1: Mean threshold and noise parameters for all flavor and their dispersion on the matrix.

at high input charge, triggering the readout and reading spurious hits. Since the injection circuit is coupled in AC to the FE, if the falling edge of the pulse is sharp enough to produce an undershoot, this can be seen as a signal.

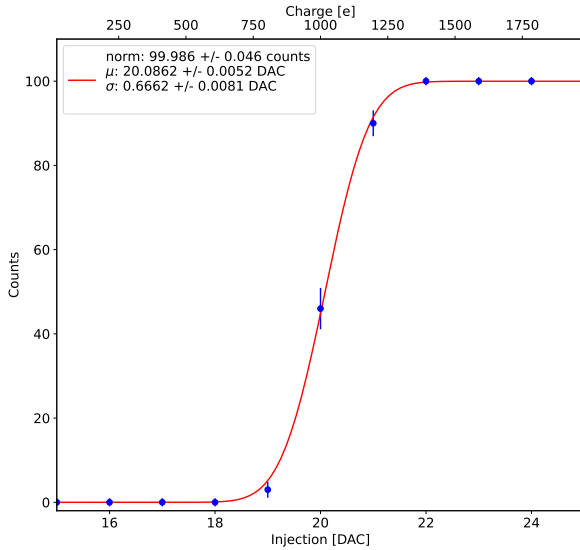


Figure 2.1: S-curve for pixel (10, 10) of the PMOS flavor (flavor B) with IDB fixed at 40 DAC. The conversion of charge injected from DAC to electrons has been performed using a nominal conversion factor of $20.3 \text{ e}^-/\text{DAC}$ *Mi sono resa conto che l'asse superiore è sbagliato. Devo rigenerare il plot*

with IDB equal to 40 DAC

Therefore I fitted the counts detected using the function in equation 2.4. Figure 2.1 shows an example of such fit for a pixel belonging to the flavor B, while in figure 2.2 are shown the 1D and 2D distributions of the parameters found. I fitted the 1D distributions with a gaussian function to found the average and RMS of the noise and the threshold for each flavor across the matrix. The results are reported in table 2.1.

In the map at the top right panel of figure 2.2 (IDB=40 DAC) a slightly lower threshold is visible in the first biasing section (columns from 0 to 14); similar structures, but extended to the entire matrix, appear more evidently when using different IDB values. The systematic threshold variation across the biasing group has not a known motivation, but one could certainly be the transistor mismatch of the biasing DAC registers IDB and ICASN, which both adjust the effective threshold (I recall that ICASN regulate the

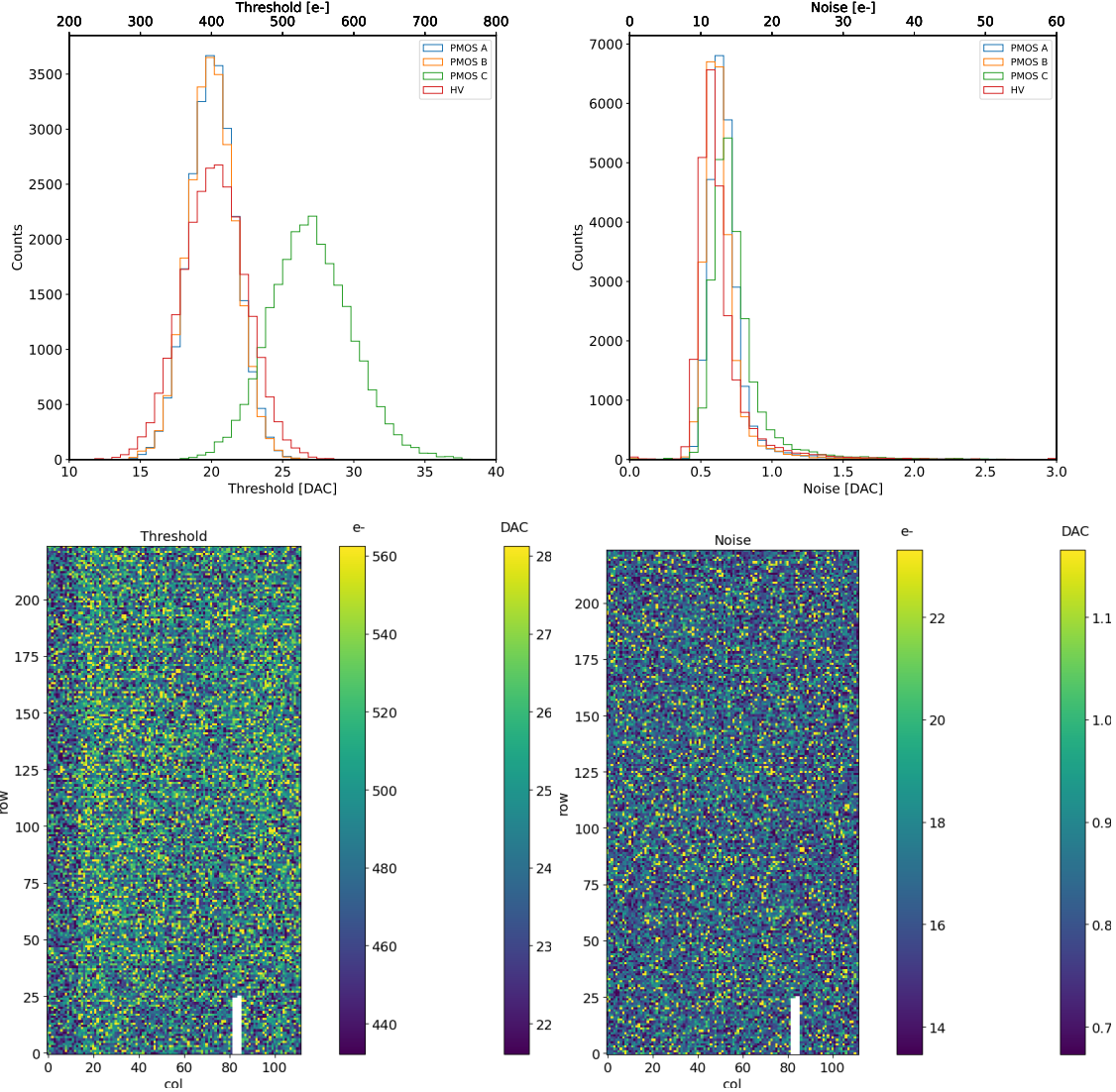


Figure 2.2: Histograms of the threshold (a) and the noise (b) found fitting the s-curve of all flavor with IDB fixed at 40 DAC. Below there are the maps of the threshold (a) and the noise (b), respectively, found fitting the s-curve with IDB fixed at 40 DAC for the PMOS flavor (B). The white pixels have the injection circuit broken.

179 baseline).

180 To verified the trend of the threshold as a function of the front end parameter IDB and
 181 find its dynamic range, I have permormed different scans changing the FE register IDB.
 182 For each IDB I have injected the whole matrix and search for the mean and the standard
 183 deviation of the threshold and noise distributions. The results are shown in figure 2.3:
 184 the blue points are the mean threhsold found whithin the matrix, while in green is shown
 185 the width of the threshold distribution, aka the threshold dispersion. While the threshold
 186 increases, the ENC decreases of $\sim 4 \text{ e-}$,which is $\sim 1/3$ of the noise at IDB=40 DAC.

187 Then, to evaluet the operation and the occupancy of the chip at different threshold
 188 I have made long acquisitions of noise at different IDB and check how the number of
 189 pixel masked changes with the threshold. The masking algorithm I have used search for
 190 pixels with rate $>10 \text{ Hz}$ and mask them. With such algorithm, in our standard condition,

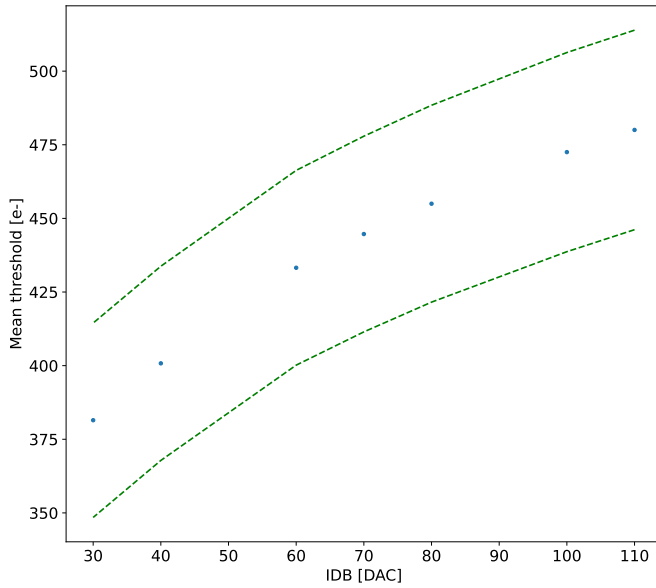


Figure 2.3: Flavor PMOS (B) with Psub-Pwell biased at -6 V. Threshold measured in electrons vs the register which sets the threshold, IDB.

191 IDB=40 DAC, a very low noise hit rate is intentionally achieved masking a dozen of pixels
 192 of the whole flavor.

193 2.1.2 Linearity of the ToT

194 I have already said in chapter ?? that TJ-Monopix1 returns an output signal proportional
 195 to the charge released by a particle in the epitaxial layer, which is the Time over Threshold;
 196 the ToT is saved as a 6-bit variable and then has a dynamic range equal to 0-64, which
 197 corresponds to 0 μ s to 1.6 μ s assuming a clock frequency of 40 MHz. When a pulse is longer
 198 than 1.6 μ s the counter rolls back to zero and there is no way to distinguish that charge
 199 from a lower one with the same ToT: that is the rollover of the ToT (2.4(a)).

200 In order to associate the ToT (in range 0-64) to the charge, a calibration of the signal
 201 is necessary. Assuming the linearity between ToT and the charge, Q can be found:

$$Q [DAC] = \frac{(ToT [au] - offset [au])}{slope [au/DAC]} \quad (2.5)$$

202 where m and q are the fitted parameters of the calibration. It is important to keep in mind
 203 that the main application target of TJ-Monopix1 is in the inner tracker detector of HEP
 204 experiments, then the main feature is the efficiency, then a rough calibration of the signal
 205 to charge is fine. The ToT information can be used both to better reconstruct the charge
 206 deposition in cluster in order to improve the track resolution, and for particle identification,
 207 especially for low momentum particles which do not reach the proper detectors.

208 The study of the output signal is made possible via the injection: since the pulses
 209 are triangular, the ToT is expected to be almost therefore, to prevent th linear. To verify
 210 this statement and study the deviations from linearity I fitted the ToT versus the charge
 211 injected for all the pixels within the matrix. In figure 2.4(b) there is an example of fit

for a pixel belonging to the flavor B, while in figure 2.5 there are the histograms and the maps of the parameters of the line-fit for all flavors with IDB fixed at 40 DAC. Here again a difference among the biasing section appears: since the slope of the ToT is related with the gain of the preamplifier (increasing the gain also increases the ToT), the mismatch is probably due to the transistor contributing to the amplification stage.

I fitted the average ToT of all the pulses recorded as a function of the pulse amplitude; data affected by rollover have been removed in order to avoid introducing a bias in the mean values. In figure 2.4 (b) are shown both the fits with a line (red) and with a second order polynomial (green): at the bounds of the ToT range values deviate from the line model. Since the deviation is lower than 1% and it only interests the region near the 0 and the 64, in first approximation it is negligible.

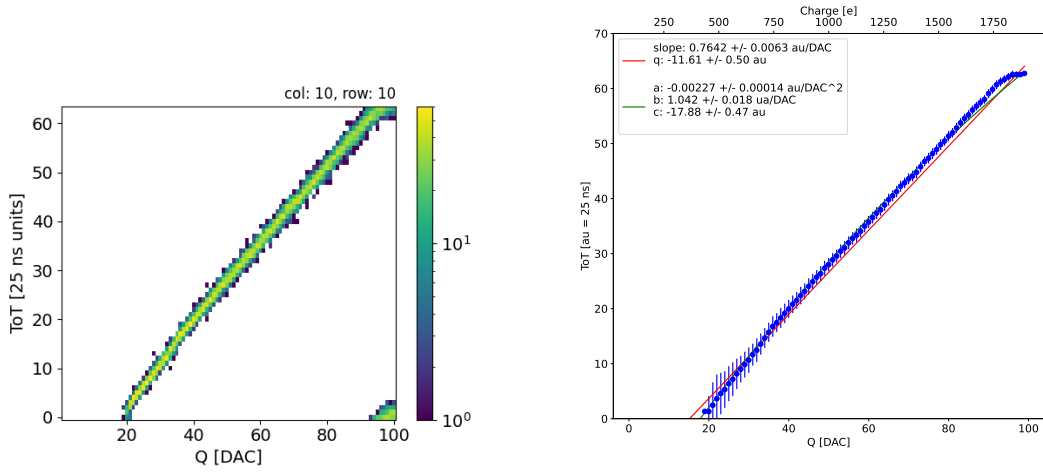


Figure 2.4: The figures refer to pixel (10,10) of the PMOS-reset flavor B with IDB fixed at 40 DAC. (a) Histogram of the injection pulses: the ToT is in range 0-64 since it is represented by 6 bit, so when achieving the 64 it rolls over back to the zero. (b) Mean ToT vs the the charge: the mean has been calculated cutted the rolling hits.

2.1.3 Calibration of the ToT

Finding a calibration for the ToT means defining a way to pass from the ToT values (0-64 clock counts) to a spectrum expressed in electrons collected. The principles of the calibration are the following: the ToT in clock counts maps (eq.2.1.2) a DAC range between the threshold and a value which depends on the pixel and generally is around 90-100 DAC. Assuming that a 0 DAC signal corresponds to 0 e⁻, if another reference point is fixed, a linear calibration function can be defined. After the calibration the ToT goes to map a charge range between the threshold and Q_{max} which is a function of the pixel and is around 2 ke⁻.

Moreover, considering that the charge injected in the FE goes to fill a capacitor C which is different from pixel to pixel, the true charge injected does not correspond to what expected assuming C equal to 230 aF, which is the nominal value. Accordingly to that, a measurement of this value provides both an absolute calibration of C and a conversion factor K to have a correspondence of the DAC signal in electrons. K and C are defined

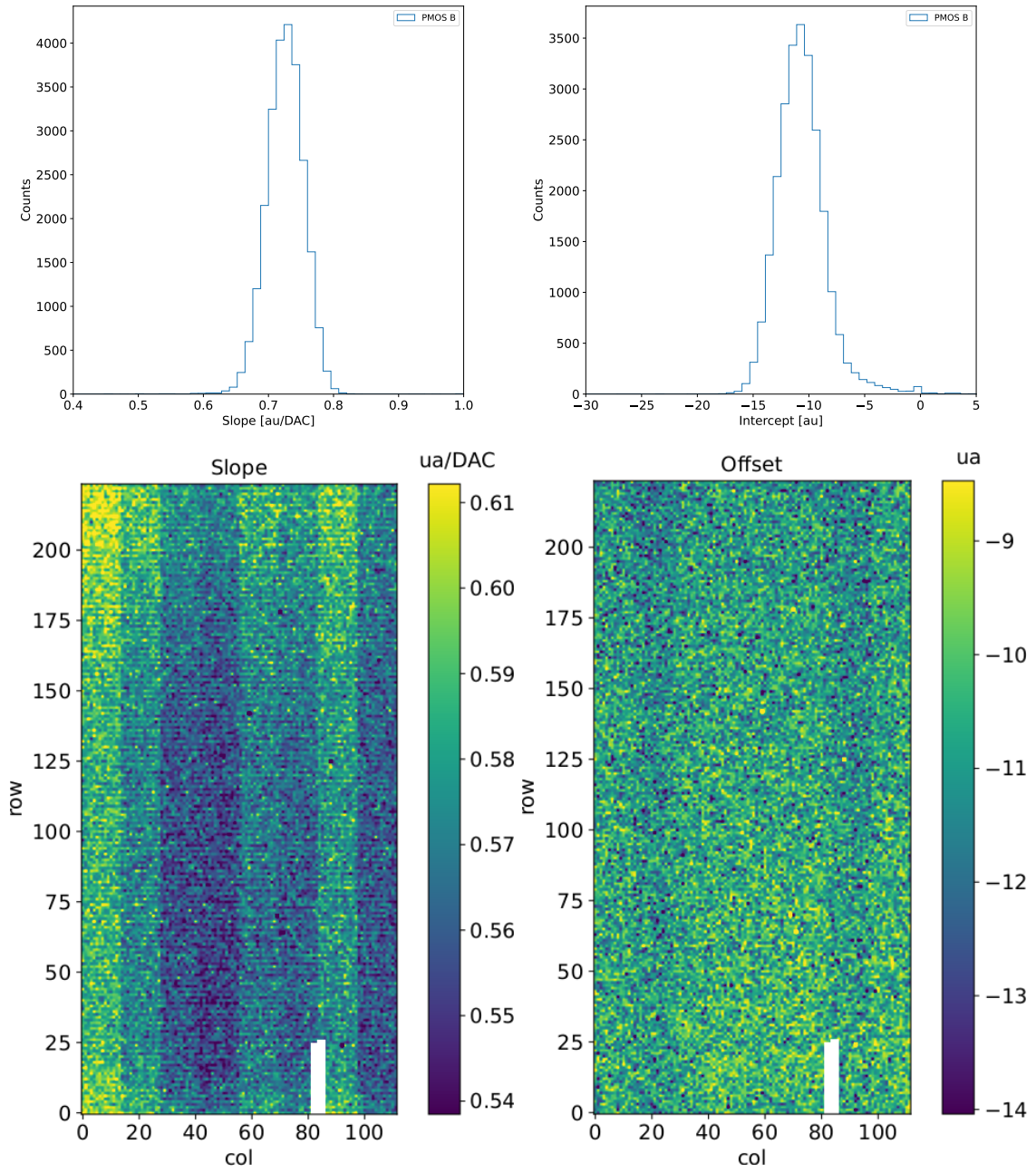


Figure 2.5: Histograms of the calibration parameters, slope (a) and offset (b), found fitting the ToT with a line, for the flavor B and with IDB fixed at 40 DAC. Maps of the calibration parameters, slope (a) and offset (b), found fitting the ToT with a line, with IDB fixed at 40 DAC.

237 respectively as:

$$K [e^- / DAC] = \frac{1616 [e^-]}{Q [DAC]} \quad (2.6)$$

238

$$C [F] = [e^- / DAC] \frac{1.6 \cdot 10^{-19} [C]}{14.7 [mV]} \quad (2.7)$$

239 where K is expected to be $20 e^- / DAC$, assuming the nominal value of C equal to $230 aF$,
240 and where 1616 is the expected number of electrons produced by the calibration source

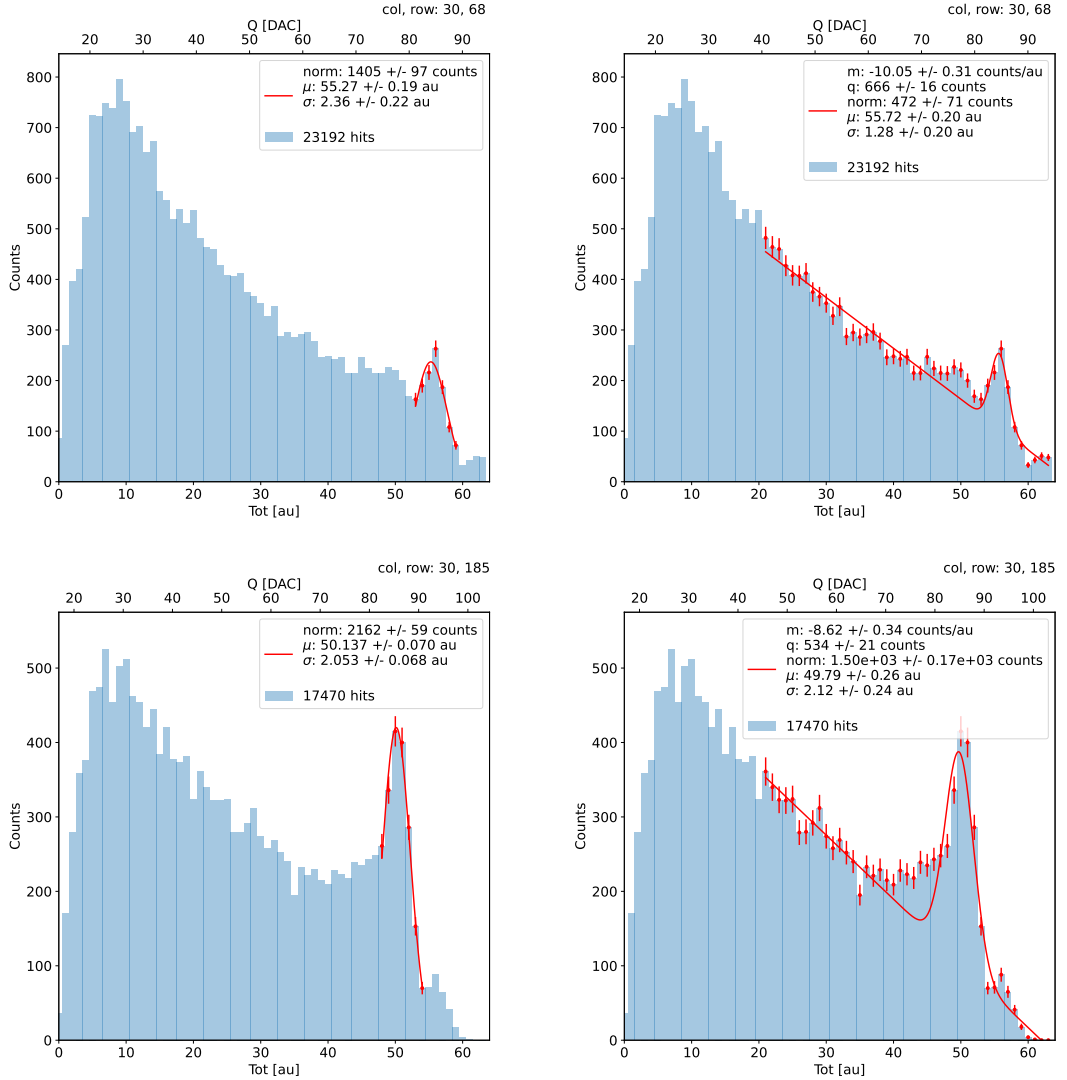


Figure 2.6: due pixel per far vedere la differenza tra i fit. Sottolinea che in rosso ci sono i bin fittati. La doppia scala utilizza le info trovate nel paragrafo precedente per il dato pixel in questione. Per avere una corrispondenza grezza in elettroni basta moltiplicare per 20 e- / dac.

used, Fe55. Fe55 is an extremely important radionuclide in the calibration of X-ray spectrometers, proportional counter and scintillator detector since it emits two X-photons during the electron capture decay: the first one (K_{α}) at 5.9 keV and the second one (K_{β}) at 6.5 keV. The K_{α} photon, which does photoelectric effect in silicon, has an absorption length $\lambda=7 \mu\text{m}$ to $8 \mu\text{m}$, and the probability of being absorbed in the $25 \mu\text{m}$ thick epitaxial layer is $\sim 0.95\%$. The electron emitted has an energy equal to the photon, so recalling that the mean energy needed to produce a couple electron-vacuum is 3.65 eV, the signal produced by the Fe55 source is expected to be 1616 e^- . In figures 2.6 are shown two histograms of the ToT spectrum of the Fe55 source for two different pixels. The peak on the right corresponds to the events with complete absorption of the charge in the depleted region, while the long tail on the left to all the events with partial absorption due to charge sharing among neighbors pixels. In order to reduce the consistent charge sharing, the pixel dimension in TJ-Monopix2 has been reduced down to $30 \times 30 \mu\text{m}^2$. The events on the right

254 side of the peak, instead, corresponds to the K_β photons. Looking at the histograms for
 255 pixel (30, 185) and (30, 69) a significant difference in the peak to tail ratio leaps out, which
 256 can be related with the position of the pixel in the matrix. In particular, because of a
 257 different charge collection property, pixels in the upper part of the matrix (rows 112-224)
 258 have a more prominent peak, while in pixels in the lower part (rows 0-111) there is a
 259 higher partial absorption. Indeed, as discussed in section ??, there is a distinction in the
 260 structure of the low dose-epi layer among the rows, in particular pixels in rows 112-224,
 261 which have a RDPW, are supposed to have a higher efficiency in the pixel corner.

262 For the calibration I needed to establish the peak position; to do that I fitted the ToT
 263 histogram of each pixel. I tested two different fit functions:

$$f(x, N, \mu, \sigma) = \frac{N}{\sigma\sqrt{2\pi}} e^{-\frac{1}{2}(\frac{(x-\mu)}{\sigma})^2} \quad (2.8)$$

264

$$f(x, m, q, N, \mu, \sigma) = m x + q + \frac{N}{\sigma\sqrt{2\pi}} e^{-\frac{1}{2}(\frac{(x-\mu)}{\sigma})^2} \quad (2.9)$$

The additional linear term in equation 2.9 is meant to model the tail due to incomplete

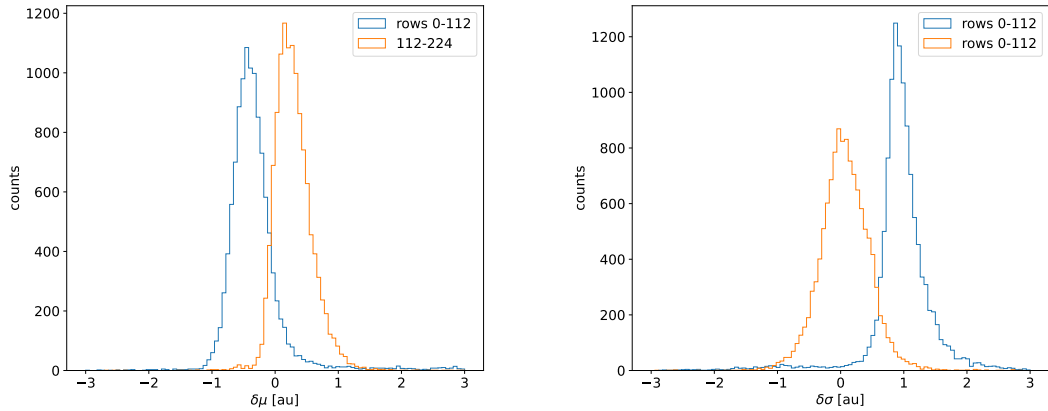


Figure 2.7: Difference between the parameters μ and σ obtained with the gaussian fit and those obtained with a gaussian plus a line. When $\mu < 0$ the fit with function 2.8 is generally worse (the peak is shifted to the left); when $\sigma < 0$, the fit with 2.9 is worse (larger sigma).

265

266 charge collection and prevent it from introducing a bias in the fitted peak position.

267 For this reason, when fitting with eq.2.9, I selected a larger region compared to the
 268 fit with eq.2.8, for which I used only a small reagion around the peak. The optimal fit
 269 region was chosen in both cases through an iterative routine: for the fit with eq.2.9 it
 270 starts from an interval including all the pixels above 20 DAC and progressively reduces it
 271 by increasing the left boundary; for the fit with eq.2.8, it starts from an interval of 5 bins
 272 around the expected peak position and reduces the interval of 1 bin at each iteration.

273 Even if the difference in the peak position between the two fit strategies is not really
 274 relevant for the purpose of the calibration, being of the order of 0.8-1.5% (2.7),it still
 275 introduces a systematic bias towards lower values due to the contribution of the tail.
 276 Indeed, we know that the sharp edge on the right must correspond to the case of complete
 277 absorption of the photon, so that, in general, the closest to this feature is the fitted peak
 278 position, the better the fit is. A poor fit tends also to overestimate the peak width. Even

279 looking at the χ^2 , the fit function 2.8 seems to be the better choice, except for a sample
 280 of pixels in the lower part of the matrix, the one with lower efficiency.

281 The resolution of the detector, which is expected to be determined by the statistical
 282 fluctuations in the number of charge carriers generated in the detector as well as by the
 283 ENC, can be compared to the observed Fe55 peak width. Ideally:

$$\sigma_{Fe} = \sqrt{ENC^2 + F \times N} \quad (2.10)$$

284 Since the number of e/h pairs produced in the sensor is 1616, recalling that F for a silicon
 285 detector is 0.115 and that the ENC measured with the injection is 12e^- , the σ_{Fe} is
 286 expected to be $\sim 18\text{e}^-$. Looking at figure 2.8 the resolution achieved with the Fe55 source
 287 seems to be much higher. A contribution we have not taken into account but is certainly
 288 relevant is the systematic overestimation of the standard deviation of the Fe55 peak: this,
 289 as I already explained, is principally due to the high background of incomplete charge
 290 collection, which broadens the fitted peak.

291 2D maps of the value of the capacity and of the conversion factor found are shown in
 292 2.9. The evident stripe-structure in the matrix shows an evident correlation among the
 293 same row; the same structure, which is also visible in the slope map of the calibration of
 the ToT (fig.??), may be related with the structure of the bias lines.

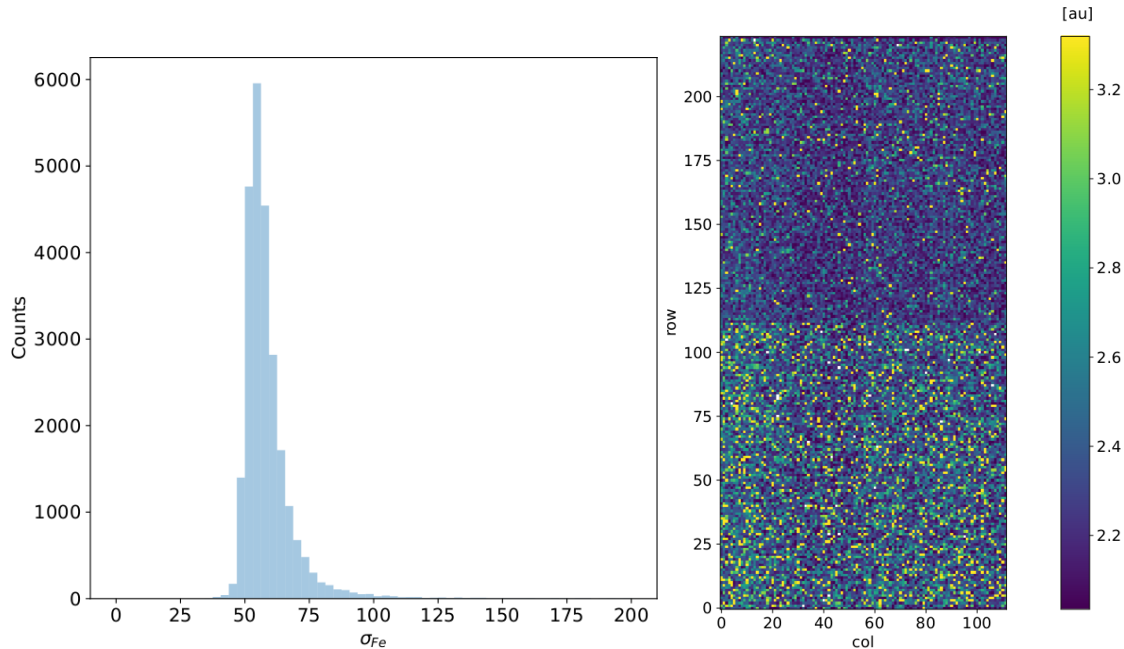


Figure 2.8: Histogram (a) and map (b) of the fitted Fe55 peak width.

294

295 HV flavor calibration

296 An attempt of calibrating the HV flavor, which is the most different from the PMOS B
 297 flavor, has been performed; however, because of the loss of signal caused by the higher
 298 capacity, we have been unable to identify the Fe55 peak in every FE and bias configuration.
 299 An example of Fe55 spectrum collected with the HV flavor is shown in figure 2.10.

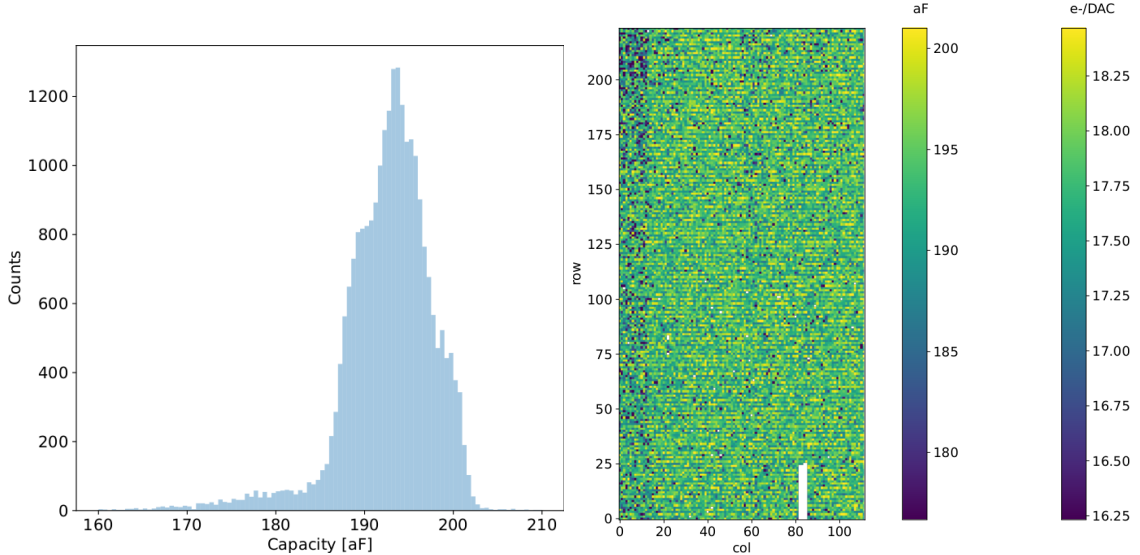


Figure 2.9: Histogram (a) and map (b) of the calibrated capacity of the injection circuit.

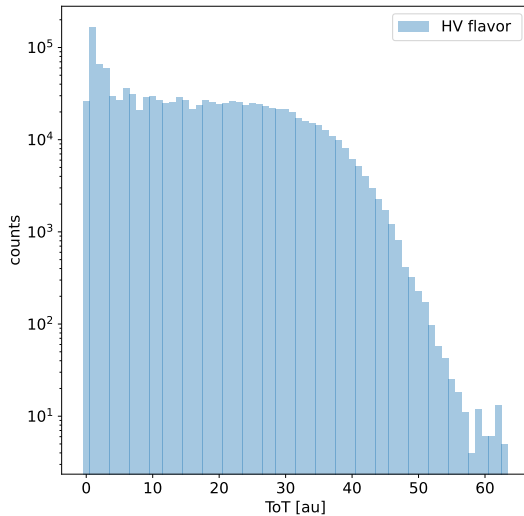


Figure 2.10: Fe55 spectrum with the HV flavor

300 2.1.4 Changing the bias

301 In order to study the behavior of the sensor as a function of the bias, I performed several
 302 injection scans in different configurations. Indeed, the thickness of the depletion region has
 303 to be considered an important parameters affecting the signal efficiency, and in particular
 304 it affects the charge released by a particle which crosses the sensor (since the signal is
 305 proportional to the thickness of the epitaxial layer). The measured output voltage ampli-
 306 tude and gain in the case of the PMOS and HV flavours are shown in figure 2.11 Given
 307 that the chip under examination has a gap in the low dose epi-layer, we were not able to
 308 change independently the bias of the substrate (PSUB) and of the p-well (PWELL), but
 309 they must be kept at the same value, differently from other chips of the same submission.
 310 Lowering the bias, the depletion region is expected to narrow and the efficiency to reduce,

	-6 V	-3 V	0 V
Threshold [DAC]	20.0 ± 1.6	21.0 ± 1.6	24.5 ± 1.8
Noise [DAC]	0.613 ± 0.075	0.625 ± 0.078	0.822 ± 0.098
Slope [au/DAC]	0.726 ± 0.027	0.707 ± 0.028	0.573 ± 0.021
Offset [au]	-10.8 ± 1.9	-11.2 ± 1.8	-11.1 ± 1.5

Table 2.2: The errors are the standard deviations of the corresponding distributions. The conversion factor from DAC to electrons is $\sim 20 \text{ e}^-/\text{DAC}$.

311 especially in the pixel corner, thus raising the threshold and the noise and decreasing the slope as a consequence of the reduction in the gain.

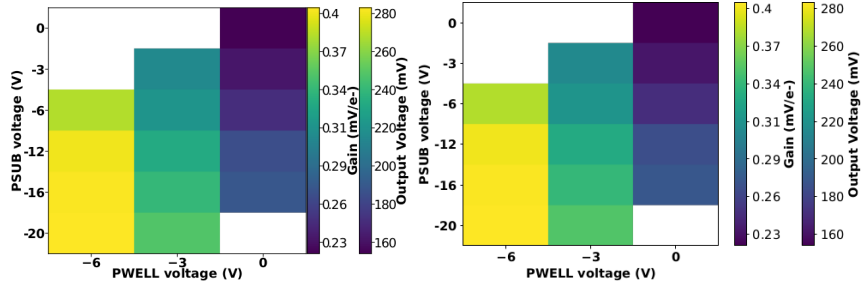


Figure 2.11: Output voltage amplitude and gain with respect to the p-well and p-substrate voltage in the case of the PMOS reset front-end (B)

312
313 In order to test the behavior of the chip when not completely depleted, I have performed
314 an injection scan with PSUB/PWELL bias at 0 V, -3 V and -6 V (results in tab.2.2), and
315 some acquisitions with the Fe55 source (fig. 2.12). There are reported the values of the
316 K_α peak position, the normalization of the events above the peak and the rate, everything
317 has been normalized to the value at the reference condition, which is with PSUB/PWELL
318 at -6 V.

319 2.1.5 Measurements with radioactive sources

320 In order to completely validate the operation of the whole sensor¹, I have performed several
321 acquisitions with radioactive sources, specifically Fe55 and Sr90Y, which is a β^- emettitor
322 with electron endpoint at 2.2 MeV, and cosmic rays. I used the data collected with Sr90
323 and cosmic rays, to study charge sharing and events with more than one hit.

324 I define *cluster* the ensamble of all the hits with the same timestamp. This is obviously
325 a coarse requirement, but it gave me the opportunity of using a simple and fast clustering
326 algorithm, which is fine when the random coincidence probability is neglibile. Defining
327 R_1 and R_2 as the two events rate, and τ as the dead time of the detector, the random
328 coincidence rate can be found:

$$R_{coinc} = R_1 \times R_2 \times \tau \quad (2.11)$$

329 As I am going to prove in the next section, the dead time strictly depends on the occupancy
330 of the matrix, even though we can assume a dead time of $\sim 1 \mu\text{m}$, which corresponds to

¹As I will discuss in chapter 3.2 these measurements serves also as a reference for the spectrum observed at the test beam

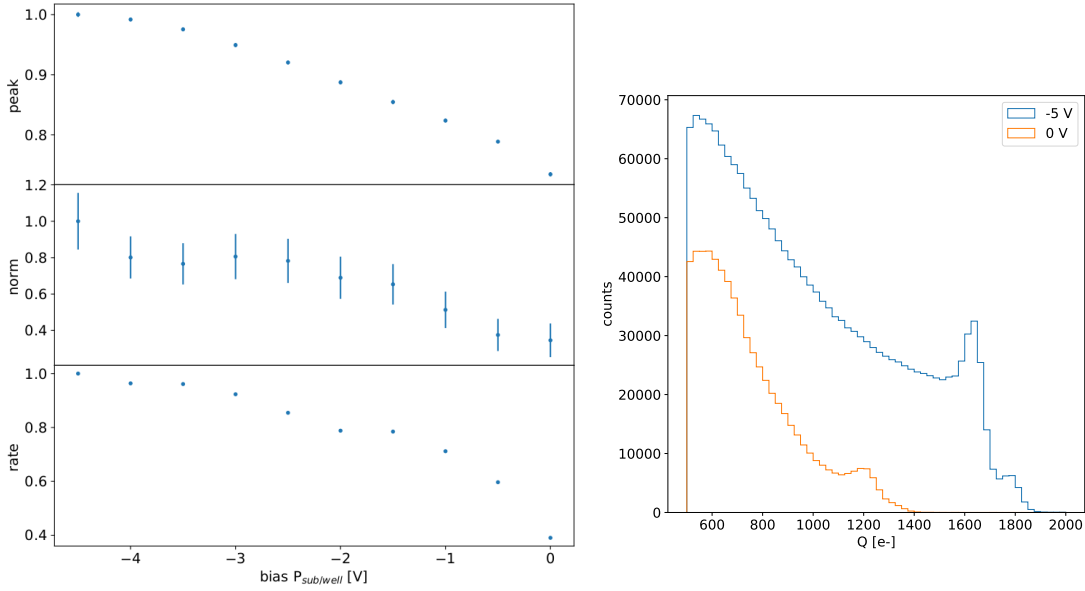


Figure 2.12: (a) Peak position, peak amplitude and rate as a function of the bias. Since during the collection of the whole data the source has been moved, it is not guaranteed that it has always had a repositioning in the same exactly place, then small the fluctuation of the rate along the decreasing trend are acceptable. The peak position and amplitude are estimated by fitting the spectrum with a gaussian in the region around the peak. (b) Fe55 spectrum at different $P_{sub/well}$ bias. The ToT values have been calibrated as explained in section. 2.1.3.

331 the mean dead time per pixel. However, if in an event a particle hits two different pixels
 332 producing a cluster, the total dead time simply doubles. Since the measured rate on the
 333 whole matrix of noise, Fe55, Sr90 and cosmic rays are \sim Hz, 3.3 kHz, 40 Hz and \sim 10 mHz²,
 334 the random coincidence probability are negligible except the one of two Fe55 events, which
 335 is 11 Hz.

336 In figure 2.13 I report the histograms of the number of pixels in the cluster and of the
 337 dimension of clusters, defined in terms of the max and min coordinates on the matrix as:

$$d = \sqrt{(y_{max} - y_{min})^2 + (x_{max} - x_{min})^2} \quad (2.12)$$

338 Looking at the shape of the histogram of the dimension, generally the Sr90 and the
 339 cosmic rays produce bigger clusters and hit a higher number of pixels, a trend that can
 340 be explained considering that the Fe55 photoelectron is much less energetic than the Sr90
 341 electron and cosmic rays. Below I have also attached a sample of hitmap of events produced
 342 by the three different sources (fig.2.14, 2.15).

343 In figures 2.18, 2.19, 2.21 are shown the distributions per different cluster dimension
 344 events, of the charge collected by a single pixel (figures on the left) and the charge collected
 345 by summing the charge collected by the pixels within the cluster (figures on the right).
 346 Since the noise rate is comparable with the cosmic rays and Sr90 ones, I have removed the
 347 single pixel events which are separately shown in figure 2.17; despite we cannot identify
 348 and selecting only the noise events, these distributions, and especially the cosmic rays
 349 one, are expected to be mostly populated by noise events. The distributions have a peak

²The cosmic rays rate at the sea level is expected to be \sim 1/cm²/s

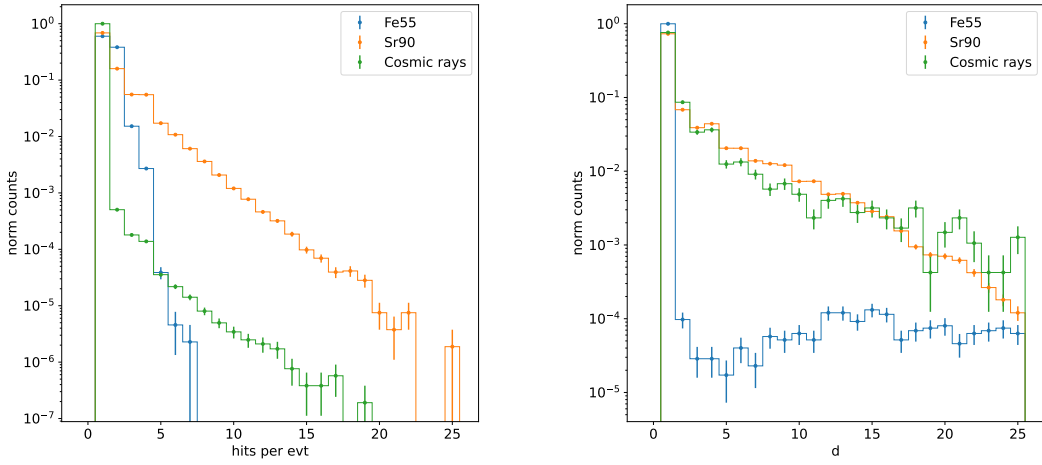


Figure 2.13: (a) Distribution of the number of hits per event with different sources. (b) Dimension of cluster defined as eq.2.1.5. Compared with the Sr90 and the cosmic rays, the Fe55 d distribution is characterized by a clear discontinuity in the cluster dimension. The very thin peak around 0 corresponds to the effective cluster, while the long tail at bigger cluster d is principally made of random coincidence.

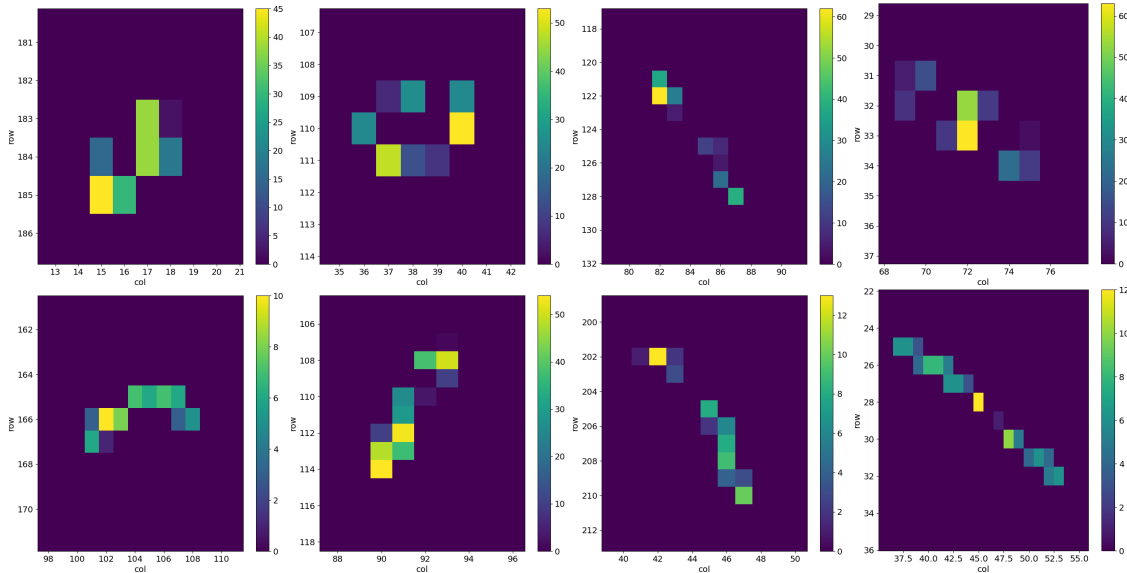


Figure 2.14: 2D histograms of the ToT in different events in an aquisition of cosmic rays.

350 around the threshold, which is compatible with the fact that the noise events typically
351 have a low ToT.

352 Looking at the spectra of Sr90 instead (fig:2.19), the maximum of the distribution of
353 the cluster charge seems to follow a linear dependence on the number of pixels hit (tab.2.3);
354 this can be accepted as a first approximation considering that the pitch ($36\text{ }\mu\text{m}$ and $40\text{ }\mu\text{m}$)
355 depending on the direction, and the epitaxial layer thickness ($25\text{-}30\text{ }\mu\text{m}$) are comparable.
356 However a more accurate model which takes into account the impact angle of the particle
357 should be developed for a more precise comparison. The charge per length covered Q/l
358 released by a particle which crosses more pixels and is not completely absorbed in the

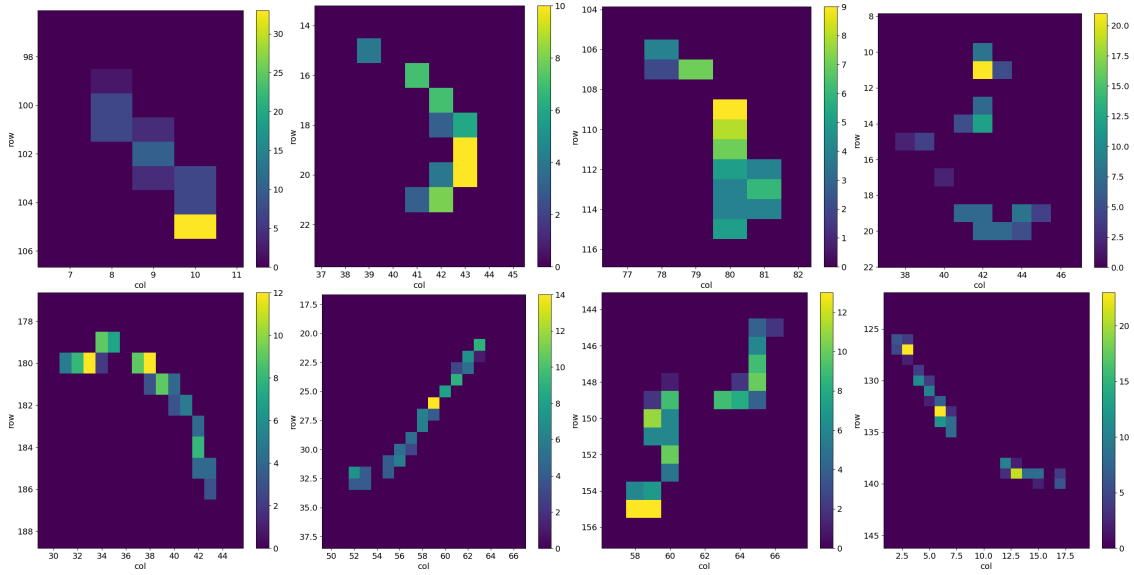


Figure 2.15: 2D histograms of the ToT in different events in an aquisition of Sr90.

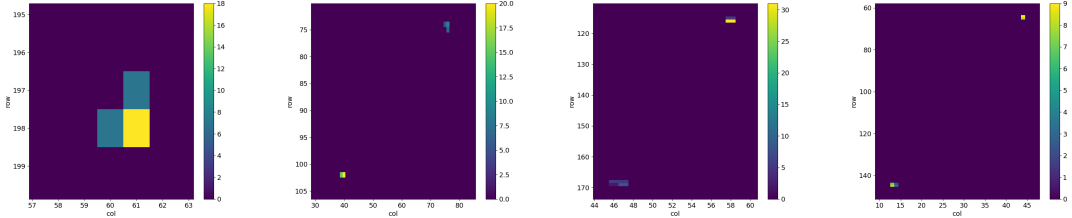


Figure 2.16: 2D histograms of the ToT in different events in an aquisition of Fe55

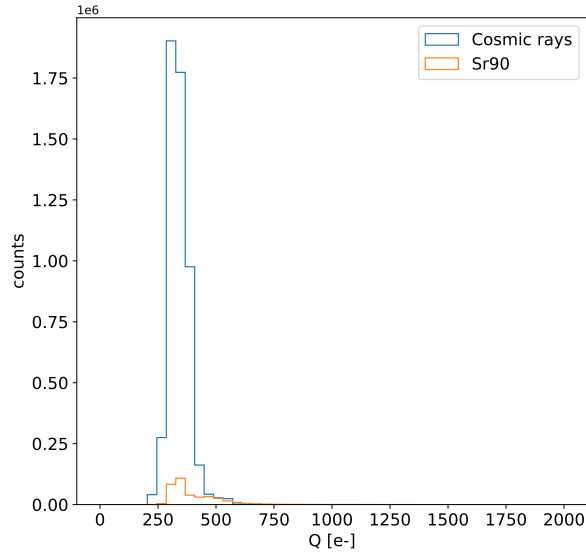


Figure 2.17: Histograms of the charge released in the pixels in events in which only a single pixel turns on.

Pixel per evt	Measured [e-]
2	950 ± 30
3	1450 ± 30
4	2050 ± 30
5	2450 ± 30

Table 2.3: Position of the maximum of the distributions in figure 2.19(b) of the summed charge released in the clusters depending on the number of pixel in the cluster.

359 sensor (fig.??) can be described by the following relation. Considering that:

$$l = \frac{t}{\cos(\lambda)} = \frac{t}{\sqrt{1 + tg^2\lambda}} = \frac{t}{\sqrt{1 + (x/t)^2}} \quad (2.13)$$

360 it can be expressed as:

$$\frac{Q}{l} = \frac{Q}{t} \sqrt{1 + (n - 1)^2 p^2 / t^2} \quad (2.14)$$

361 where p/t is the ratio between the pitch and the epitaxial layer thickness, and then it
 362 is different in the x and y directions ($40 \mu\text{m}$ and $36 \mu\text{m}$ respectively). Taking as value of
 363 p/t 1.52, which is the mean on the two axis, the value of Q/l expected by the scaling
 364 relation and the charge actually measured in the acquisition with the Sr90 are illustrated
 365 in table 2.3; because of the decision of cutting the single pixel events in order to have
 366 a clean sample, the expected value has been obtained by the two hits cluster dividing
 367 the charge by 2. By the inversion of the formula ??, the single pixel charge is then
 368 expected to be 522 e-. FORSE DATO CHE LA MASSIMA CARICA RILASCIATA
 369 SCALA LINEARMENTE CON IL NUMERO DI PIXEL NON SCRIVEREI QUESTA
 370 COSA? O MAGARI LA METTO COME CORREZIONE? The measured value has been
 371 obtained by the maximum of the distributions in the left plots in ??

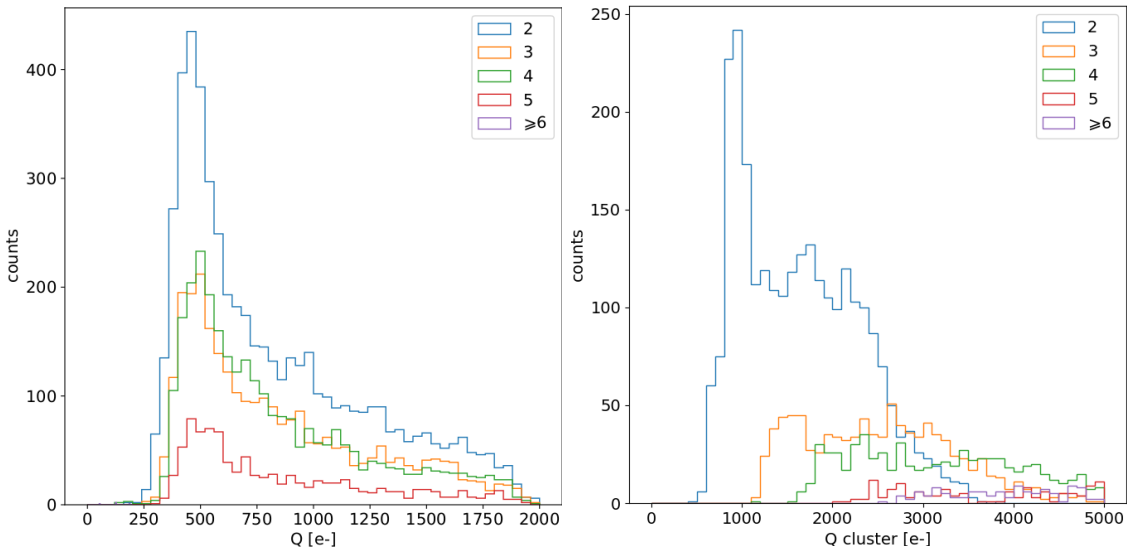


Figure 2.18: Acquisition of cosmic rays with IDB=40 DAC

372 Regarding the Fe55, the bump in the cluster spectrum at $\sim 1616 \text{ e-}$ corresponds to
 373 photons which had converted at the boundary of nearby pixels thus sharing their charge
 374 among them. Starting from 4-pixels clusters the peak moves to the right: this is due to

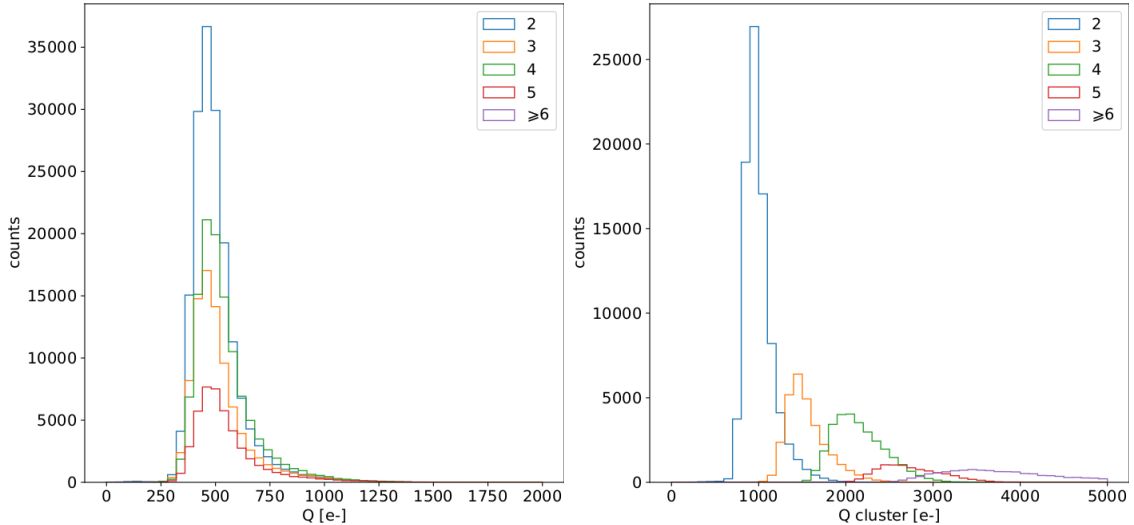


Figure 2.19: Acquisition of Sr90 with IDB=40 DAC

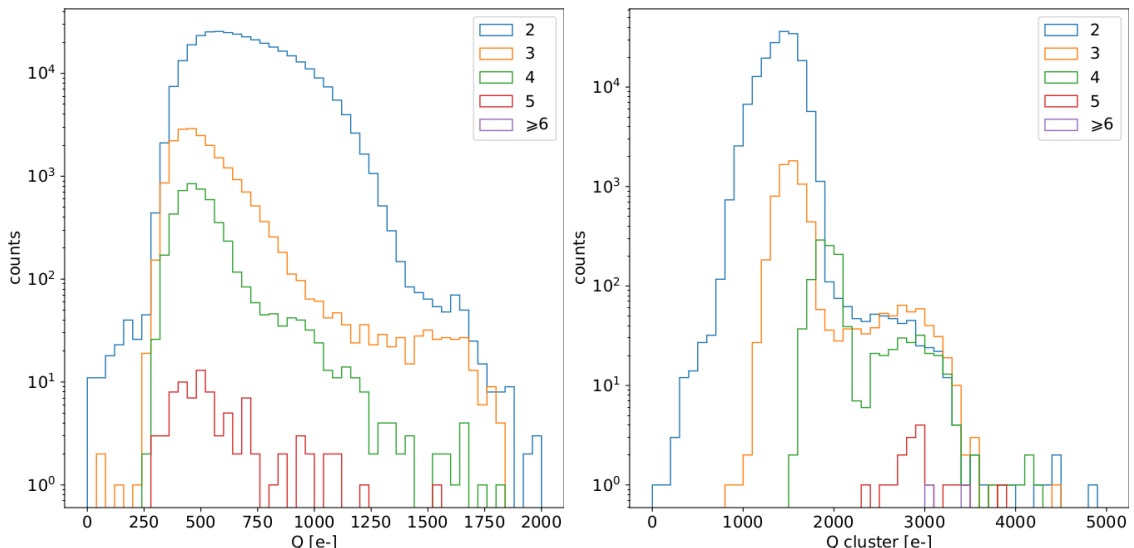


Figure 2.20: Acquisitions with radioactive source and cosmic rays at IDB=40 DAC.

Figure 2.21: Acquisition of Fe55 with IDB=40 DAC

375 the fact that the cluster with more than 3 pixels are principally random coincidence events
 376 Fe55-Fe55 or Fe55-noise. Recalling that the noise typically just exceeds the threshold and
 377 then has low ToT, the peak position in the spectrum ?? of 4-pixel cluster can be explained
 378 admitting that one of the four pixel is a noise signal. The shoulder on the right, instead,
 379 which have an edge at about 3200 e- corresponds to the events with coincidence of two
 380 photons. Looking at the charge on the single pixel spectrum (fig.??), instead, a small
 381 bump can be seen around 1616 e-: these events correspond to photons which released
 382 almost all the charge on one pixel.

383 2.1.6 Dead time measurements

384 The hit loss is due to analog and digital pile up: the first one occurs when a new hit
 385 arrives during the pre-amplifier response, the second instead when the hit arrives while

386 the information of the previous hit has not yet been transferred to the periphery. Since the
 387 pre-amplifier response has a characteristic time \sim ToT, the dead time τ_a introduced by it
 388 will be at most 1.6 μ s; using the IRESET and VRESET FE parameters the reset time can
 389 be lowered down, but as explained in section ?? it must be longer than the preamplifier
 390 characteristics time in order to not cut the signal. Regarding the latter contribution instead,
 391 since only one hit at a time can be stored on the pixel's RAM, until the data have completed
 392 the path to get out, the pixel is paralyzed. Moreover since there is no storage memory
 393 included on TJ-Monopix1 prototypes, the digital dead time τ_d almost corresponds to the
 394 time needed to trasmit the data-packets off-chip.

395 The exportation of data from pixel to the EoC occurs via a 21-bits data bus, therefore
 396 only one clock cycle is needed and the dead time bottleneck is rather given by the
 397 bandwidth of the serializer which trasmits data off-chip from the EoC. In our setup the
 398 serializer operates at 40 MHz, thus to transmit a data packet (27-bit considering the ad-
 399 dition of 6 bits to identify the double-column at the EoC) at least 675 ns are needed. For
 400 what we have said so far, the R/O is completely sequential and therefore is expected a
 401 linear dependence of the reading time on the number of pixels to read:

$$\tau = 25 \text{ ns} \times (\alpha N + \beta) \quad (2.15)$$

402 where α and β are parameters dependent on the readout chain setting.

403 To test the linearity of the reading time with the number of pixels firing and to measure
 404 it, I have used the injection circuit which allows me choosing a specific hit rate: I made
 405 a scan injecting a fix number of pulses and each time changing the number of pixels
 406 injected. Indeed the injection mode allows fixing not only the amplitude of the pulse,
 407 which corresponds to the charge in DAC units, but also the time between two consecutive
 408 pulses (DELAY). The hit rate then corresponds to 25 ns/DELAY.

409 Unfortunately a high random hit rate on the matrix cannot be simulated by the in-
 410 jection because of the long time (\sim ms) needed to set the pixel registers of the injection;
 411 then I was forced to specify at the start of the acquisition the pixels to inject on, and for
 412 convenience I chose those on a same column. In figure 2.22 is shown the dependence of
 413 the efficiency on the DELAY parameter in two different cases. For the 5 pixels example
 414 the efficiency goes down the 90% at a DELAY of \sim 185 clock counts, which corresponds
 415 to 4.625 μ s and to a rate of 216 kHz, while in the 10 pixels example, the efficiency goes
 416 under the 100% at \sim 380 clock counts, which corresponds to 9.5 μ s and to a rate of 105 kHz.
 417 From the efficiency curves I have then looked for the time when the efficency decreases.
 418 In figure 2.23(a) is shown the dead time per pixels as a function of N with different R/O
 419 parameters configuration, the meaning of which is explained in chapter ???. The default
 420 value suggested by the designer of the chip are reported in table 2.4; moving too much
 421 the readout parameters from the default ones, the readout does not work properly, and no
 422 hits can be read at all. The problem probably stays in the firmware setting of the readout
 423 which are specially fixed for our chip **Sul repository, nei commenti ci sono altri valori pos-
 424 sibili per il FREEZE, ma avevamo detto che probabilmente sono relativi ai setting di altri
 425 chip.** Despite the single pixel reading time does not depend on the position on the pixel
 426 matrix, whithin a clock count which is \sim 25 ns, and it is equal to 106 clock counts, since
 427 the τ_d critically depends on the pixel position on the matrix: in particular the reading
 428 sequence goes from row 224 to row 0, and from column 0 to column 112, making the pixel
 429 on the bottom right corner the one with the longest dead time.

430 Furthermore to test that there is no dependece of the digital readout time from the

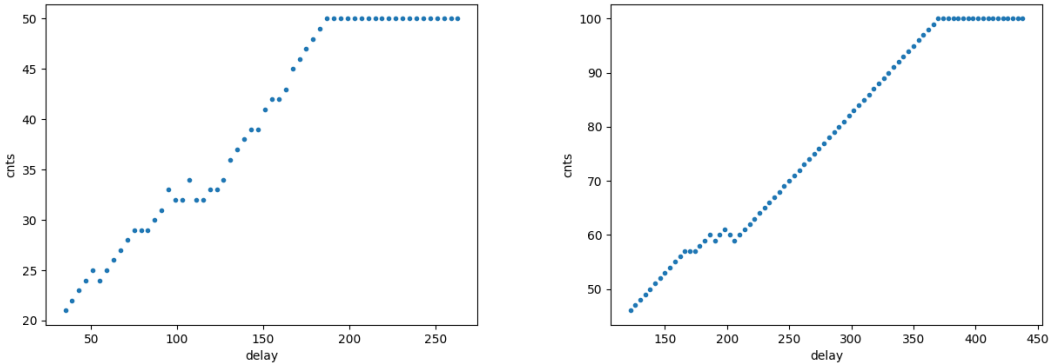


Figure 2.22: Efficiency vs the DELAY parameters. (a) I made a scan injecting 5 pixels with 50 pulses for each DELAY configuration and (b) 10 pixels with 100 pulses for each DELAY

Parameter	Value [DAC]	Value [μ s]
START_FREEZE	64	1.6
STOP_FREEZE	100	2.5
START_READ	66	1.65
STOP_READ	68	1.7

Table 2.4: Default configuration of the R/O parameters

431 charge of the pulse, I have try to change the amplitude of the pulse injected, but the
 432 parameters found were consistent with the default configuration ones. No difference in
 433 the α and β coefficients has been observed between the two case. Referring to eq.2.15, the
 434 factor α is proportional to the difference (STOP_FREEZE - START_READ), while the
 435 offset β lies between 5 and 15 clock counts.

436 The readout time found by this test is so long because in the prototypes no paralleliza-
 437 tion of the informations (with the instruction of more serializer for example) and no
 438 storage memory are included; this feature are typically added in the final prototypes. An
 439 example closely linked to TJ-Monopix1 is OBELIX: it will include on the chip a storage
 440 buffer to optimize the dead time and to keep a low occupancy even at high fluence.

441 2.2 ARCADIA-MD1 characterization

442 Unfortunatly the characterization of MD1 has not yet been completed because of some
 443 problems with the functionality of the first chip we received on which we have been able
 444 to make only a few electrical and communication test in order to test the operations of the
 445 FPGA and the breakount board (BB). We asked for another chip then but we, due to
 446 delay in the extraction and the bonding of the wafer, have received it one week ago; an
 447 exhaustive characterization and testing of the new chip have been going on in the clean
 448 room on the INFN, and I am going to show here only some preliminary results.

449 The problem with the broken chip occurs when it is biased, in particular, when the HV
 450 voltage is lowered down 0V, the sensor requires too much power and a too high current
 451 draw sets. We have discussed the problem with the designers of the chip whose helped

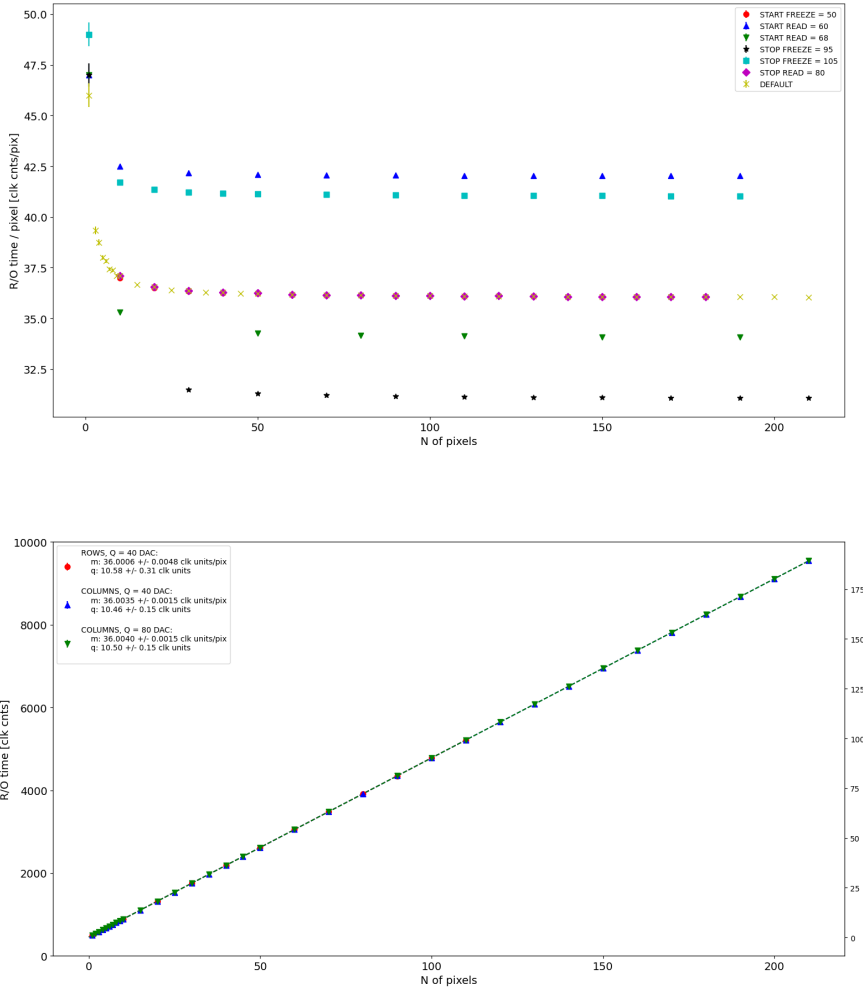


Figure 2.23: (a) Readout time per pixel as a function of the number of pixel injected obtained with different FE setup. (b) Readout time as a function of the number of pixels injected obtained injecting pulses with amplitude of 80 DAC (green), of 40 DAC on the same row (red) and on the same column (blue).

us indentifying the motivation of the break: the chip has been glued using too much conductive tape and hence have a short-circuit between the sides and the back, which makes impossible the biasing. Unfortunately, since both the sensor and the FE require at least -10 V to work properly, no measurement was possible except the acquisition of the noise in the FE circuit.

The second chip we received is a minid2, that is a "mini demonstrator" from the second submission. The two have the same charateristics but the minid2 is smaller than the MD1, in particular it only have 32×512 pixels, instead of 512×512 .

Up to now we used the injection circuit in order to make a threshold scan on a few pixels: differently from the TJ-Monopix1's charaterization where we performed a scan changing the injection charge of the pulse, with the minid2 we have instead changed the threshold (whose register is VCASN) keeping the charge of the pulse fixed. For each threshold we inject 100 pulses of amplitude $10 \mu\text{s}$. The dependence of the efficiency on the threshold for two pixels is shown in figure 2.25. Even if the behavior is reasonable, as the

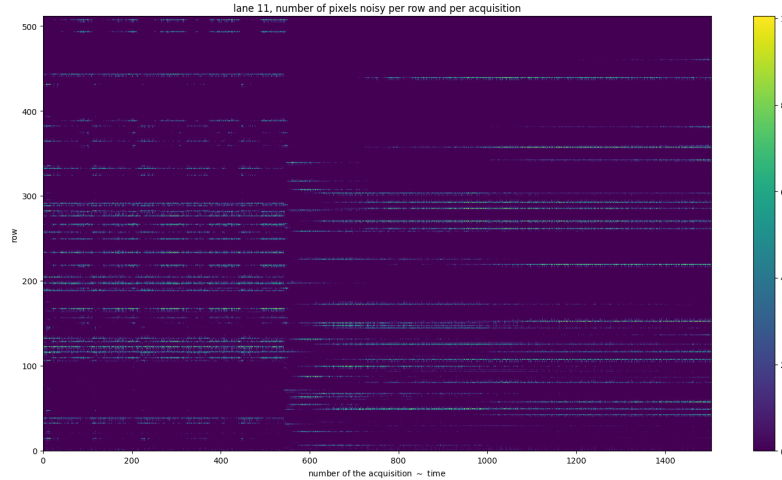


Figure 2.24: Noise in the front end circuit depending on the bias road across the matrix was recorded.

466 threshold is reduced the efficiency becomes higher, it is possible that the bias (-50 V) is
not enough to full deplete the sensor, since the counts does not reach the 100% steadily.

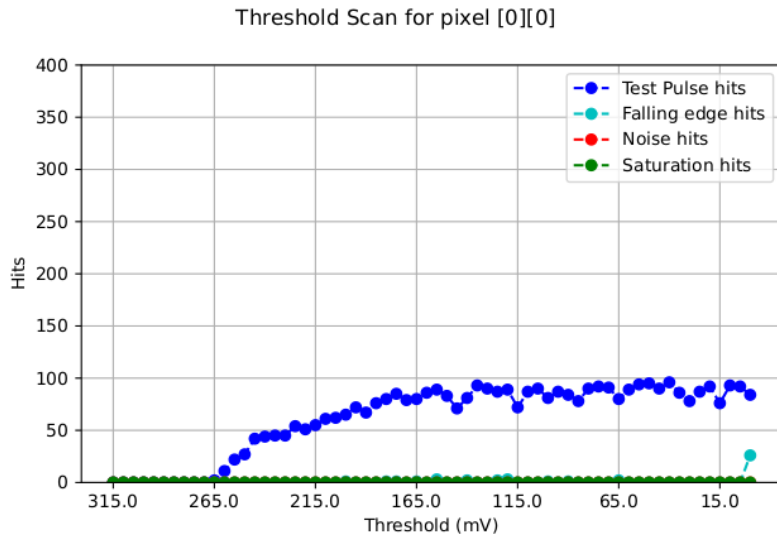


Figure 2.25: Threshold scan on the pixel (0,0). The sensors is polarized with $\Delta V = -50$ V.

467
468 The value of the SNR and the ENC Charge injection circuit uses $C_{inj} = 2.325$ fF The
469 SNR, the ENC and the threshold dispersion on the matrix are expected to be respectively
470 ~ 90 , $3 e^-$ and $\sim 35 e^-$ with a detector capacity of 7 fF, that is about the capacity expected
471 for the detector. The injection capacity is expected to be ~ 2.325 fF, and in this condition
472 the the minimum and maximum signals generated are respectively 0.08 fC and 2.6 fC.

473 Substantial differences have been observed with VCASN=40 DAC in both the efficiency
474 and the threshold among the sections; this suggests that with this particular FE config-
475 uration there is a big threshold dispersion on the matrix. The hitmap of an acquisition
476 with the Fe55 source is shown in figure 2.26: the whole MD1 matrix with only the bottom
477 region (32 rows) working is represented in (a), while in (b) there is a zoomed hitmap. The

478 rate seen within the region 8 (green region in the figure (a)) is compatible with the rate
of the same radioactive source measured with TJ-Monopix1, that it ~ 3.3 kHz. Looking to

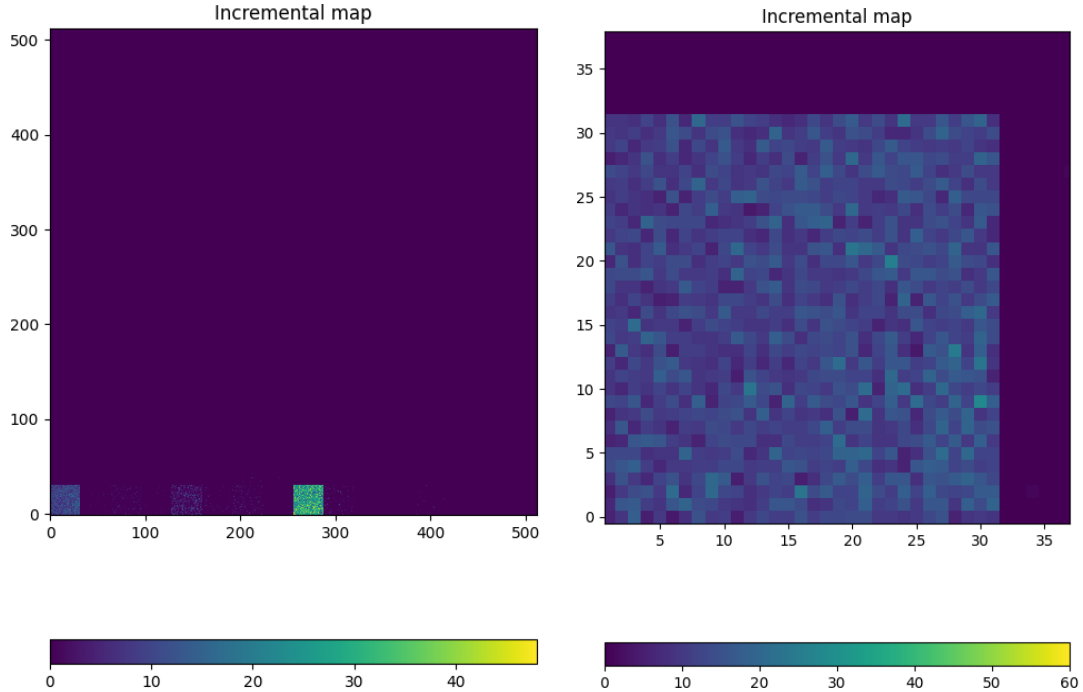


Figure 2.26: Fe55 acquisition with VCASN=40 DAC. (a) All the matrix 512×512 is plotted even if the minid2 has only the rows in range 0-32. (b) A zoom on the first section (col 0-32).

479
480 the Sr90 acquisitions (fig.2.27) many clusters and tracks can be immidiately distiguished,
confirming what observed with TJ-Monopix1.

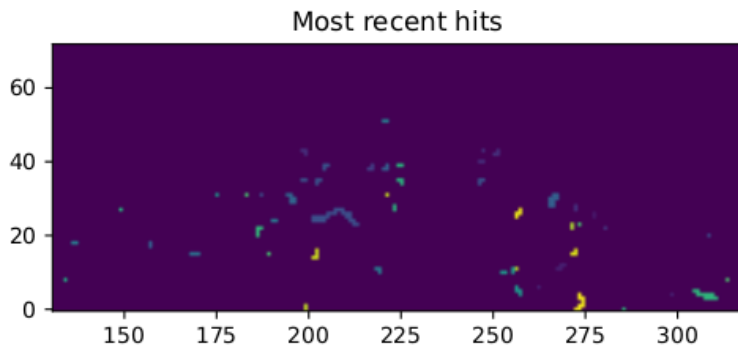


Figure 2.27: Sr90 acquisition with VCASN=40 DAC. The different colours are related with the time of arrival of the hits: in yellow the most recent hits, while in blue the old ones.

481

482 Chapter 3

483 Test beam measurements

484 During August 2022 a testbeam took place in Santa Chiara hospital in Pisa, where a
485 new accelerator designed for both medical research and R&D on FLASH-RT, and for this
486 reason called "ElectronFlash", have been installed a few months ago. The motivation
487 of the testbeam measurements were testing TJ-Mopopix1 at high dose rate with a focus
488 on investigating the possibility of the application in radiotherapy. Despite this particular
489 device does not seem fitting the requirements imposed for that application, especially
490 regarding the readout time, the measurements have been useful since help us characterizing
491 the setup for future advance, and also give us the possibility of a complete characterization
492 of the chip.

493 Given that in medical physics the dose is the standard parameter to characterize the
494 beam, because of its obvious relation with the damage caused in the patient, I am going
495 to explain the meaning of it by the point of view of the instrumentation. Infact, when
496 interacting with measuring systems a more common and useful parameter is the rate or
497 the fluence of particles. The conversion between the two quantity can be found thinking to
498 the definition of dose: it is the concentration of energy deposited in tissue as a result of an
499 exposure to ionizing radiation. Assuming total absorption of electrons in water, defined
500 by law as the ordinary reference medium, the dose can be expressed as:

$$D[Gy] = \frac{NE[eV]}{\rho[g/cm^3]A[cm^2]x[cm]} \quad (3.1)$$

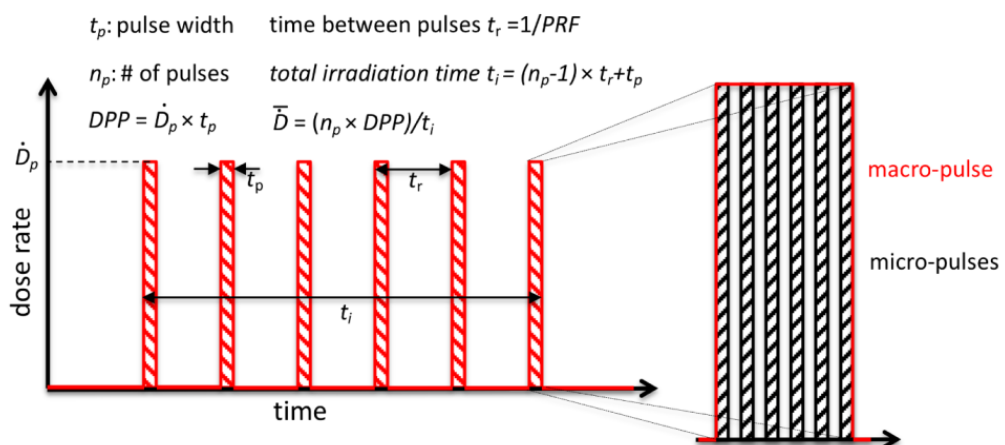


Figure 3.1: Typical beam structure of a beam used in electron radiotherapy

\bar{D}	Dose rate (mean dose rate for a multi-pulse delivery)	0.005-10000 Gy/s
\dot{D}	Intra pulse dose rate (dose rate in a single pulse)	0.01-1 10^6 Gy/s
DDP	Dose in a single pulse	0.04-40 Gy
PRF	Pulse repetition frequency	1-350 Hz
t_p	Pulse width	0.2-4 μ s
n	Number of pulses	single/pulse train

Table 3.1: The parameters that can actually be set by the control unit are the PRF, DDP, t_p and n (in particular the modality of singular irradiation or pulse train), while the other changes consequently.

501 After having applied the conversion of the energy from eV to J and noticed that $E/\rho x$
 502 roughly corresponds to the stopping power S of electrons in water, a simple estimation of
 503 the dose released in water is:

$$D[Gy] = 1.602 \cdot 10^{-10} N[cm^{-2}] S[MeV cm^2/g] \quad (3.2)$$

504 3.1 Apparatus description

505 In order to shield the outdoor from ionizing radiation the accelerator is placed in a bunker
 506 inside the hospital. The bunker has very thick walls of cementum and both the control
 507 units of the accelerator and of the detector were placed outside in a neighbor room.

508 3.1.1 Accelerator

509 The ElectronFlash accelerator is an electron Linear Accelerator (LINAC) with two energy
 510 configurations, at 7 MeV and 9 MeV, and it can reach ultra high intensity (40 Gy/pulse)
 511 keeping the possibility of accessing many different beam parameters and changing them
 512 independently from each other, a characteristic that makes it almost unique worldwide
 513 and which is fundamental for research in FLASH-RT, both for the medical aspects¹ and
 514 for the studies on detectors. The accelerator implements the standard beam structure
 515 used in RT with electrons (fig. 3.1), that is a macro pulse divided in many micropulses;
 516 the parameters used to set the dose and their range of values settable by the control unit
 517 is reported in table 3.1.

518 The accelerator is also provided of a set of triod cannons ~ 1.2 m long and with diameters
 519 in range from 1 cm to 12 cm and a collimator that can be used as beam shaper to
 520 produce a squircle shape. The triode, which is made by plexiglass, must be fix to the gun
 521 during the irradiation and is needed for producing, via the scattering of electrons with it,
 522 an uniform dose profile (fig.3.2) which is desired for medical purpose.

523 3.1.2 Mechanical carriers

524 The tested detector consists in one chip, the Device Under Test (DUT), mounted on
 525 a board and connected to FPGA with same arrangement of figure ???. These boards
 526 have been positioned vertically in front of the triode on a table specifically built for the

¹For example, it is not yet really clear the dependence of the efficacy of the FLASH effect on the whole beam parameters

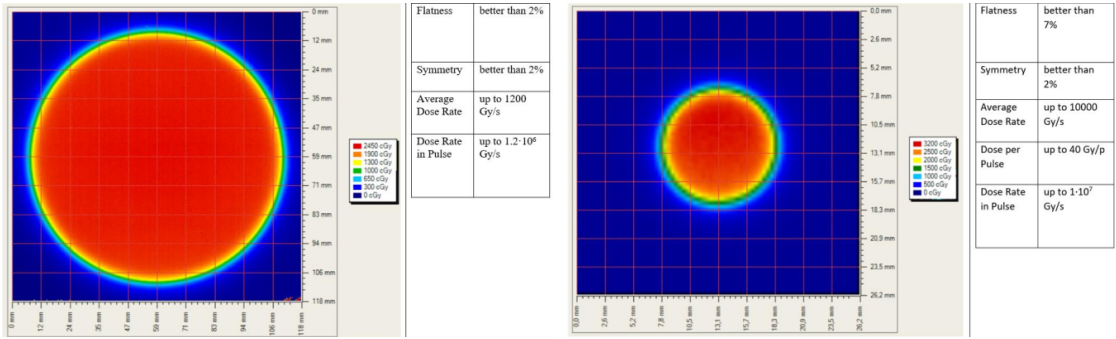


Figure 3.2: Two example of x-y isodose curves for two different triodes, 10 cm and 1 cm respectively, reported by the producer in the manual with the specific of the accelerator (S.I.T. - Sordina IORT Technologies S.p.A.). With the smaller collimator the dose rate in pulse is comparatively higher.

527 testbeam. The tree board have been enclosed in a box of alluminium with a window on
 528 the DUT and with the required holes at the side to enable the biasing via cables and the
 529 connection with the DAQ provided via ethernet cable. A trigger signal coming from the
 530 control unity and syncronized with the pulses emitted from the beam has been also sent to
 531 the FPGA. This digital signal cannot be considered a real trigger, since the TJ-Monopix1
 532 prototype has been designed to be triggerless, but its Time of Arrival (ToA) had allowed
 533 the reconstruction of the correct timing during the analysis.

534 In order to shield the sensor from the whole particles emitted from the gun, two
 535 alluminium collimators have been fabricated: one has been positioned at the triode exit
 536 while the other in front of the DUT. The collimators are $t=32$ mm thick and have a
 537 diameter d equal to 1 mm: assuming a beam divergence bigger than $d/t=1/32 = 1.8^\circ$,
 538 which is the case, the collimator at the triode output was supposed to work as a point
 539 source and to reduce the rate on the DUT of a factor at least $4 \cdot 10^{-4}$. The second one,
 540 being near the DUT, was instead supposed to shield the sensor from the electrons which
 541 have passed the first one, except for a region of 1 mm^2 configurable using *come si chiamano*
 542 *quei cacciavitini per settare la posizione? sliding trimmer?*.

543 3.2 Measurements

544 Because of the dead time of TJ-Monopix1 it is not possible resolving the bunch sub-
 545 structure and almost no one pixel can read more than a hit per bunch. I recall, indeed,
 546 that the dead time per pixel depends on the location on the readout priority chain and
 547 for each pixel $\lesssim 1 \mu\text{s}$ are needed; therefore, assuming a pulse duration of $4 \mu\text{s}$, only a few
 548 pixels at the top of the priority chain (placed at the upper left on the matrix) can fire a
 549 second time, as they can be read a first time before the end of the pulse and then can be
 550 hit again.

551 Since resolving the single electron track is impossible, a way this sensor could be used
 552 in such context is reducing its efficiency and taking advantage of the analog pile up and
 553 of the linearity of the analog output (ToT), in order to see a signal produced not by the
 554 single particle but by more electrons. Reducing the efficiency and the sensibility of the
 555 sensor is essential in order to decrease the high charge signal produced in the epitaxial
 556 layer and mitigating the saturation limit: the smaller the output signal produced by a

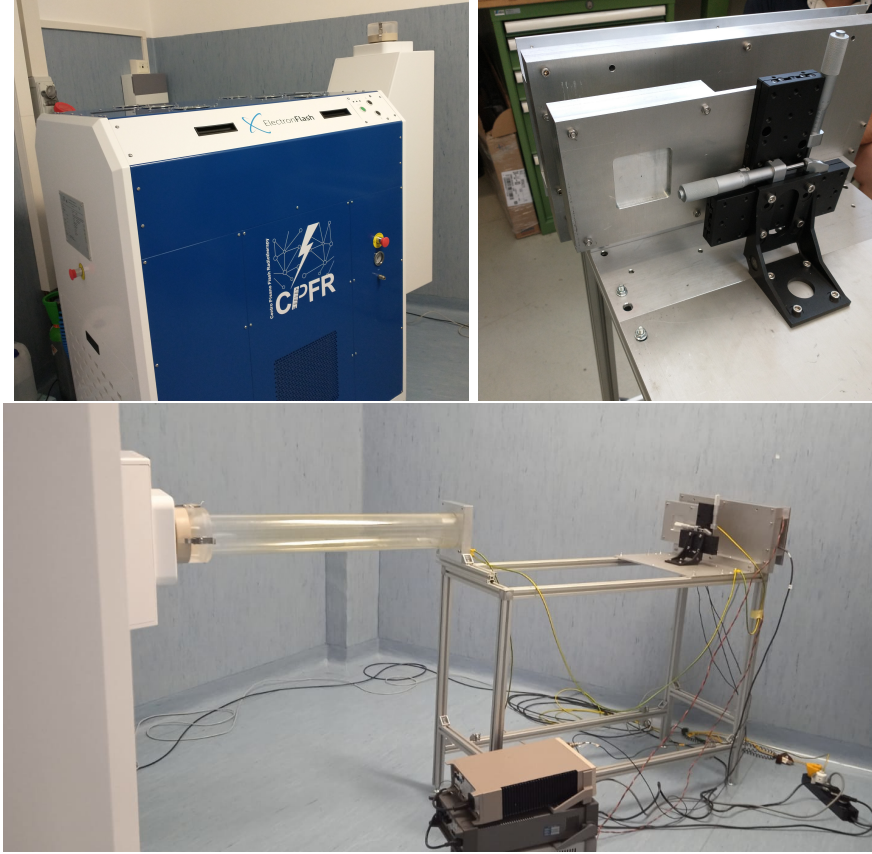


Figure 3.3: Experimental set up. (a) ElectronFlash accelerator: a rotating gantry allows the gun orientation from 0° to 90° (horizontal /vertical). (b) Collimator and DUT box. (c) Whole structure mounted: we used the 10 cm diameter and 1.2 m long triode; the DUT which is in the box behind the two collimators is connected to the power supply units.

557 particle and the higher the fluence the detector can cope with. There is an obvious limit in
 558 this context that is the ToT rollover, indeed, the signal stop giving information when this
 559 value has been overridden and is no more bijective. With the standard configuration of
 560 the FE parameters and the epitaxial layer completely depleted, a MIP produces a charge
 561 at the limit of representation with a 6-bit ToT; to obtain smaller output signals one can
 562 operate on the reduction of the gain.

563 Recalling the results in section 2.1.4, I have shown that concerning the PMOS flavor
 564 B, reducing the bias from -6 V to 0 V brings a reduction of efficiency down to 40 %, and a
 565 reduction in the gain of a factor $\sim 1/3$, while the reduction of the gain of the preamplifier
 566 allows a reduction of **circa 10, ma da controllare**.

567 In order to take advantage of the analog pile up and integrating the charge, for
 568 simplicity assume of two electrons, the second one must hit the pixel before the ToT goes
 569 under the threshold. The general condition is then $\overline{\Delta T} < \overline{ToT}$, but if a high $P_\mu(n \geq 1)$ is
 570 required, a lower $\overline{\Delta T}$ may be desired:

$$P(n \geq 1) = \sum_{n=1}^{\infty} \frac{e^{-\mu} \mu^n}{n!} = 1 - P(0) = 1 - e^{-\mu} \quad (3.3)$$

571

$$\mu = \frac{\overline{ToT}}{\overline{\Delta T}} \quad (3.4)$$

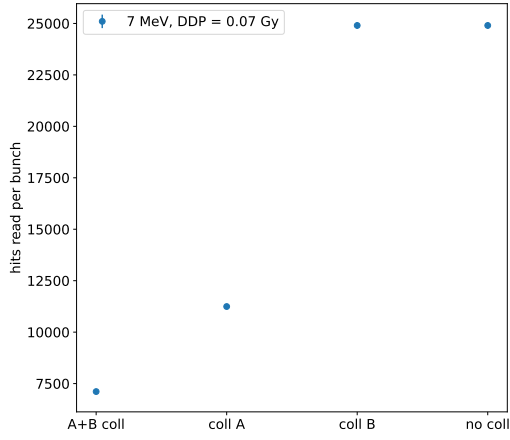


Figure 3.4: Mean number of hits read per bunch at DDP=0.07 Gy, with all the possible setup condition: with both the collimator, with only the collimator far from the chip (A), with only the collimator near the chip (B), and without any collimator.

572 If a $P_\mu(n \geq 1) = 99\%$ then the $\overline{\Delta T}$ must be $\sim 0.22 \overline{ToT}$. The ToT is in range [0,64] but
 573 since the rollover must be avoided, the \overline{ToT} must be lower than 32, and then the minimum
 574 rate on the pixel must be 1.25 MHz.

575
 576 During the testbeam many runs have been performed, spanning the energy, the dose
 577 per pulse and the four possible configurations with/without the collimators. We have
 578 collected data with the PMOS flavor A in the standard configuration: with the PWELL
 579 and PSUB biased at -6 V and set the standard default FE parameters reported in table
 580 ???. During all the data acquisitions we have selected on the control unit of the accelerator
 581 pulses with t_p of 4 μ m and with the smallest PRF settable, which is 1 Hz, in order to start
 582 in the most conservative working point excluding the digital pile up of events from different
 583 bunches. In these conditions, even if the whole matrix turns on, the total readout time
 584 corresponds to $25000 \times 1 \mu s = 25 \text{ ms}$ is still lower than the time between two consecutive
 585 pulses. In figure 3.4 is shown the mean number of hits read during one accelerator pulse
 586 in different setup conditions.

587 The readout starts with the trailing edge of the first pulse going down the threshold:
 588 about 50 clk=1.25 μ s after this moment the FREEZE signal is sent to the whole matrix,
 589 and the transmission of the data to the EoC begins. The hits read during the FREEZE
 590 signal are the ones whose TE occurred before the start of the FREEZE and which have the
 591 TOKEN signal high; the ones, instead, whose TE occur during the FREEZE are stored in
 592 the pixel memory until the end of the FREEZE. At this point a second readout starts and
 593 a second FREEZE is sent to the matrix. An example of the two sub-pulses corresponding
 594 to an electron bunch is shown in figure 3.5: in the acquisition we injected 5 pulses with
 595 both the collimators mounted on the table. Looking at the spectrum we can see that the
 596 second sub-pulse has a populated tail on the right; this is due to the fact that the hits
 597 which arrive before the start of the first FREEZE but have a long ToT that falls during
 598 the FREEZE, are read at the second sub-pulse.

599 The 2D histograms in figure 3.5, reveal an important characteristics of our setup: in

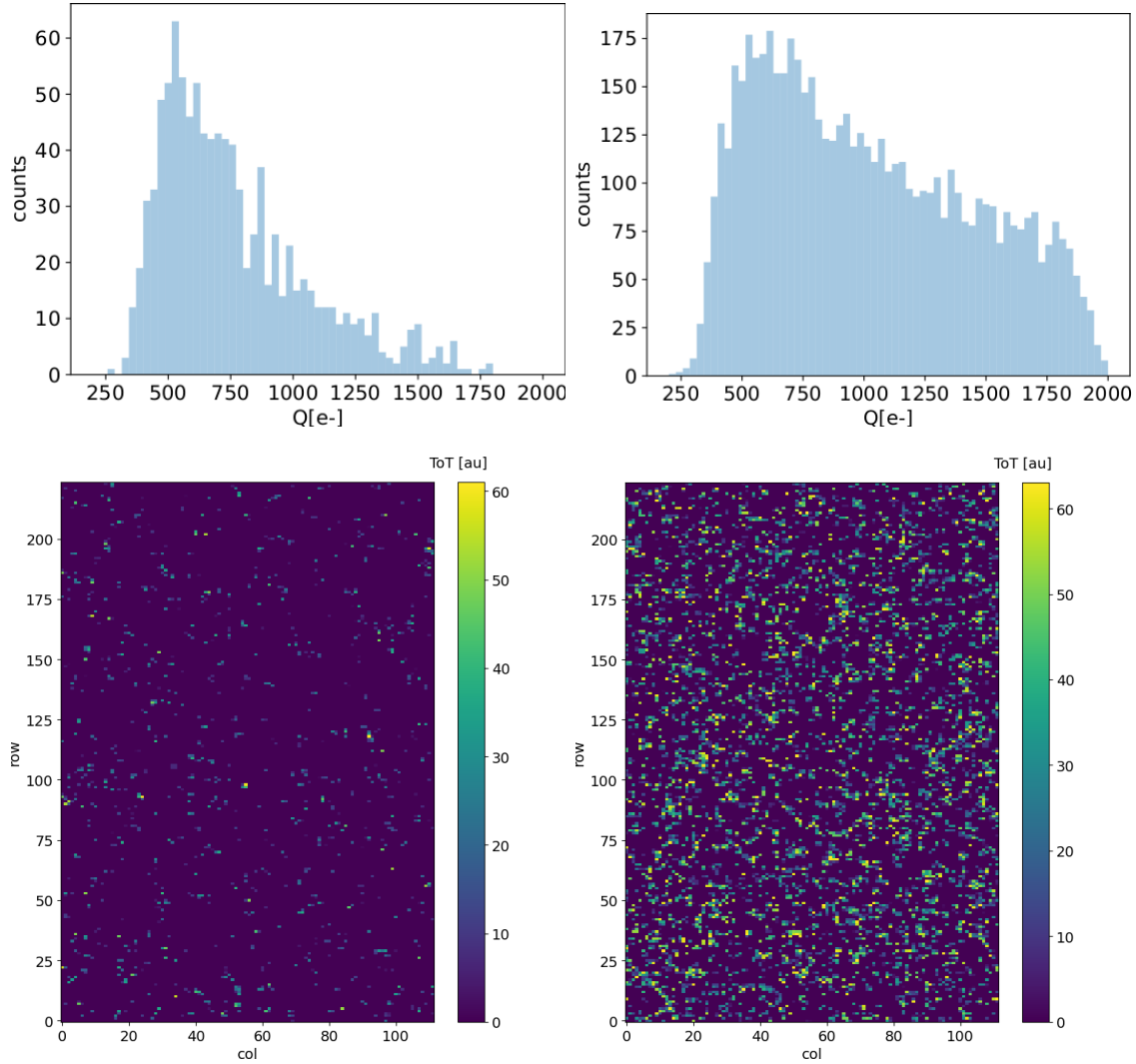


Figure 3.5: Acquisition with both the collimators: 5 pulses at $DDP=0.07\text{ Gy}$. (a) Spectrum of the charge released in the sensor: to apply the conversion I used the information found in the previous chapter. (b) 2D histogram of the ToT of the hits arrived in the sub-pulses.

fact, being uniform and not showing disomogenities, it follows that the collimators do not shield all the particles. We supposed that this was due to a Bremsstrahlung photon background higher than expected but a full verification of that and the analysis of the data is still going on. In figure 3.6, instead, the histograms with a higher DDP value is shown; in the example the matrix turns on completely, but again this happens in two different consecutive read chain.

When we have put aside the collimators, instead, the fluence increase a lot and the two-pulses substructure no more appears (fig. 3.7), but, because of the high attivity of the matrix, after each readout new hits with a fixed ToT were induced due to crosstalk. This problem had already been observed on other prototypes of TJ-Monopix1, and thanks to a simulation it has been observed that the main source of crosstalk is the voltage drop of the pre-amplifier ground as a result of the accumulated current that is drawn from the discriminator.

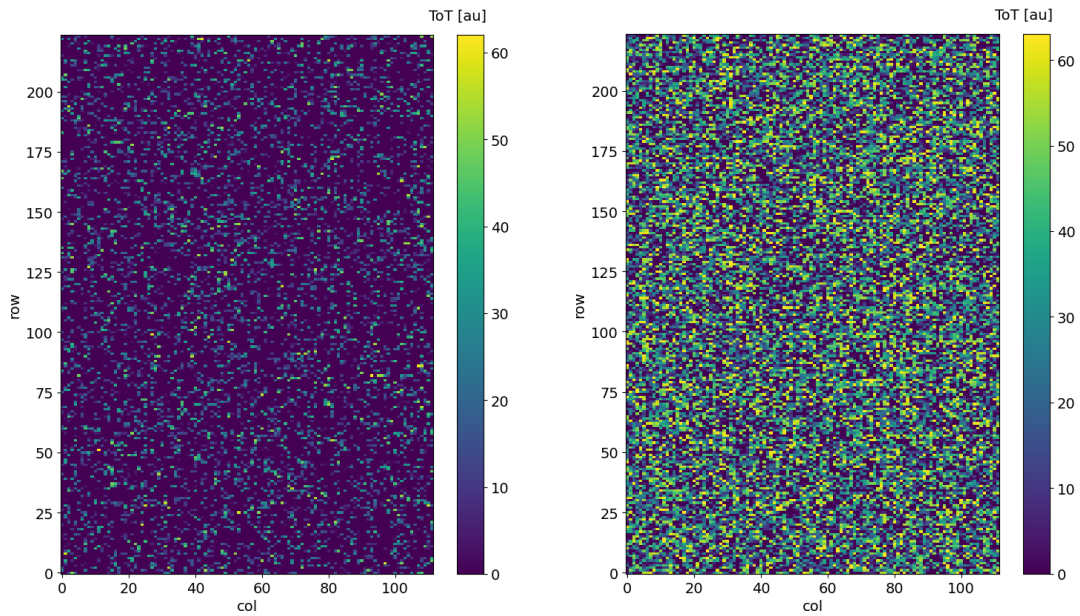


Figure 3.6: Acquisition with both the collimators: 5 pulses at $DDP=0.6\text{ Gy}$. 2D histogram of the ToT of the hits arrived in the sub-pulses. Compared with the previous maps, since the DDP is much higher, more pixels turn on.

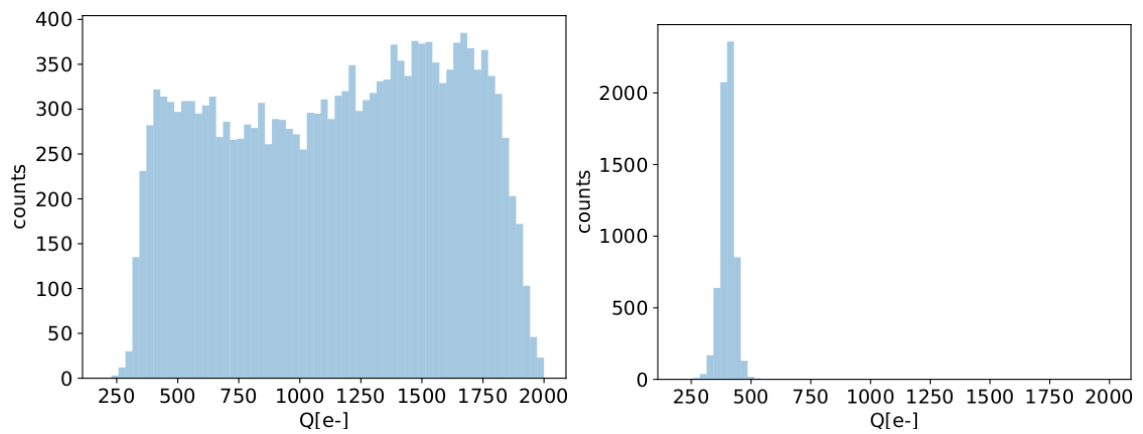


Figure 3.7: Acquisition without any collimator: 5 pulses at $DDP=0.04\text{ Gy}$.

613 Bibliography

- 614 [1] W. Snoeys et al. “A process modification for CMOS monolithic active pixel sensors
615 for enhanced depletion, timing performance and radiation tolerance”. In: (2017).
616 DOI: <https://doi.org/10.1016/j.nima.2017.07.046>.
- 617 [2] H. Kolanoski and N. Wermes. *Particle Detectors: Fundamentals and Applications*.
618 OXFORD University Press, 2020. ISBN: 9780198520115.
- 619 [3] E. Mandelli. “Digital Column Readout Architecture for 10.1109/NSSMIC.2009.5402399
620 the ATLAS Pixel 0.25 um Front End IC”. In: (2002).
- 621 [4] M. Garcia-Sciveres and N. Wermes. “A review of advances in pixel detectors for
622 experiments with high rate and radiation”. In: (2018). DOI: <https://doi.org/10.1088/1361-6633/aab064>.
- 624 [5] C. Marinas. “The Belle-II DEPFET pixel detector: A step forward in vertexing in the
625 superKEKB flavour factory”. In: (2011). DOI: [doi:10.1016/j.nima.2010.12.116](https://doi.org/10.1016/j.nima.2010.12.116).
- 626 [6] J. Baudot. “First Test Results Of MIMOSA-26, A Fast CMOS Sensor With Inte-
627 grated Zero Suppression And Digitized Output”. In: (2010). DOI: [doi:10.1109/NSSMIC.2009.5402399](https://doi.org/10.1109/NSSMIC.2009.5402399).
- 629 [7] A. Dorokhov. “High resistivity CMOS pixel sensors and their application to the
630 STAR PXL detector”. In: (2011). DOI: [doi:10.1016/j.nima.2010.12.112](https://doi.org/10.1016/j.nima.2010.12.112).
- 631 [8] Giacomo Contin. “The STAR MAPS-based PiXeL detector”. In: (2018). DOI: <https://doi.org/10.1016/j.nima.2018.03.003>.
- 633 [9] Nolan Espplen. “Physics and biology of ultrahigh dose-rate (FLASH) radiotherapy:
634 a topical review”. In: (2020). DOI: <https://doi.org/10.1088/1361-6560/abaa28>.
- 635 [10] Fabio Di Martino et al. “FLASH Radiotherapy With Electrons: Issues Related to
636 the Production, Monitoring, and Dosimetric Characterization of the Beam”. In:
637 *Frontiers in Physics* 8 (2020). ISSN: 2296-424X. DOI: [10.3389/fphy.2020.570697](https://doi.org/10.3389/fphy.2020.570697).
638 URL: <https://www.frontiersin.org/articles/10.3389/fphy.2020.570697>.
- 639 [11] M. Dyndal et al. “Mini-MALTA: Radiation hard pixel designs for small-electrode
640 monolithic CMOS sensors for the High Luminosity LHC”. In: (2019). DOI: <https://doi.org/10.1088/1748-0221/15/02/p02005>.
- 642 [12] M. Barbero. “Radiation hard DMAPS pixel sensors in 150 nm CMOS technology
643 for operation at LHC”. In: (2020). DOI: <https://doi.org/10.1088/1748-0221/15/05/p05013>.
- 645 [13] K. Moustakas et al. “CMOS Monolithic Pixel Sensors based on the Column-Drain
646 Architecture for the HL-LHC Upgrade”. In: (2018). DOI: <https://doi.org/10.1016/j.nima.2018.09.100>.

- 648 [14] I. Caicedo et al. “The Monopix chips: depleted monolithic active pixel sensors with
649 a column-drain read-out architecture for the ATLAS Inner Tracker upgrade”. In:
650 (2019). DOI: <https://doi.org/10.1088/1748-0221/14/06/C06006>.
- 651 [15] D. Kim et al. “Front end optimization for the monolithic active pixel sensor of the
652 ALICE Inner Tracking System upgrade”. In: *JINST* (2016). DOI: doi:10.1088/
653 1748-0221/11/02/C02042.
- 654 [16] L. Pancheri et al. “A 110 nm CMOS process for fully-depleted pixel sensors”. In:
655 (2019). DOI: <https://doi.org/10.1088/1748-0221/14/06/c06016>.
- 656 [17] L. Pancheri et al. “Fully Depleted MAPS in 110-nm CMOS Process With 100–300-
657 um Active Substrate”. In: (2020). DOI: 10.1109/TED.2020.2985639.